

Thermal shallow water models of geostrophic turbulence in Jovian atmospheres

Emma S. Warneford^{1, a)} and Paul J. Dellar^{1, b)}

OCIAM, Mathematical Institute, University of Oxford, Radcliffe Observatory Quarter, Oxford, OX2 6GG, United Kingdom

(Dated: 13 November 2013)

Conventional shallow water theory successfully reproduces many key features of the Jovian atmosphere: a mixture of coherent vortices and stable, large-scale, zonal jets whose amplitude decreases with distance from the equator. However, both freely decaying and forced-dissipative simulations of the shallow water equations in Jovian parameter regimes invariably yield retrograde equatorial jets, while Jupiter itself has a strong prograde equatorial jet. Simulations by Scott and Polvani [Geophys. Res. Lett. **35**, L24202] have produced prograde equatorial jets through the addition of a model for radiative relaxation in the shallow water height equation. However, their model does not conserve mass or momentum in the active layer, and produces mid-latitude jets much weaker than the equatorial jet. We present the thermal shallow water equations as an alternative model for Jovian atmospheres. These equations permit horizontal variations in the thermodynamic properties of the fluid within the active layer. We incorporate a radiative relaxation term in the separate temperature equation, leaving the mass and momentum conservation equations untouched. Simulations of this model in the Jovian regime yield a strong prograde equatorial jet, and larger amplitude mid-latitude jets than the Scott and Polvani model. For both models, the slope of the non-zonal energy spectra is consistent with the classic Kolmogorov scaling, and the slope of the zonal energy spectra is consistent with the much steeper spectrum observed for Jupiter. We also perform simulations of the thermal shallow water equations for Neptunian parameter values, with a radiative relaxation time scale calculated for the same 25 millibar pressure level we used for Jupiter. These Neptunian simulations reproduce the broad, retrograde equatorial jet and prograde mid-latitude jets seen in observations. The much longer radiative time scale for the colder planet Neptune explains the transition from a prograde to a retrograde equatorial jet, while the broader jets are due to the deformation radius being a larger fraction of the planetary radius.

Submitted 7 May 2013, accepted 20 December 2013. *Physics of Fluids* **26** 016603 doi:10.1063/1.4861123

I. INTRODUCTION

Large-scale zonal (east-west) jets are observed in a wide range of geophysical and planetary flows, most impressively in the atmospheres of the gas giant planets: Jupiter, Saturn, Uranus, and Neptune. In recent years, evidence has been put forward that zonal jets also exist in the Earth's oceans.^{1,2} Vasavada and Showman³ recently reviewed the current state of observational data, theory, experiments and simulations related to Jupiter's atmosphere. Almost all data comes from remote observations, which reveal a highly turbulent cloud deck containing long-lived coherent vortices, such as the Great Red Spot, which are transported around the planet by an alternating pattern of around 30 zonal jets. Figure 1(a) shows Jupiter's mean zonal wind profile, as derived from feature tracking in images taken by the Voyager 2 and Cassini missions.^{4,5} The similarity of these two profiles, taken from missions over 20 years apart, demonstrates the remarkable stability of Jupiter's zonal winds, and the presence of a broad, prograde equatorial jet. Figure 1(b) shows the corresponding zonal wind profile for Neptune taken from Hubble Space Telescope observations.⁶

Our only data from below the Jovian cloud deck come from the descent by the Galileo probe at 6.4° North, within the equatorial jet. The (prograde) zonal wind speed increases from around 90 ms⁻¹ at 0.7 bars to around 170 ms⁻¹ at 4 bars, then remains roughly uniform to the last received data at a depth of 22 bars.⁷ This pressure corresponds to a depth of 150 km, a tiny fraction of Jupiter's radius (see Table I). It remains a matter of conjecture whether the surface winds and jets are confined to a shallow weather layer, or extend deep into the interior. The deep interior is almost certainly convecting, since Jupiter radiates substantial internal energy,^{3,8,9} but the Galileo probe data suggest at least some stable stratification down to a depth of 22 bars.¹⁰ Observations of waves propagating away from the impact points of Shoemaker–Levy comet debris provide further evidence of stable stratification in the visible uppermost atmosphere.^{11,12} A transition like that between the terrestrial troposphere and stratosphere may be linked to latent heat released by condensation of water vapor.^{8,13} Some support for the shallow layer hypothesis is provided by fully three-dimensional simulations using general circulation models (GCMs) adapted for Jovian parameter regimes. Simulations in spherical annuli occupying the top 10%, or even 6%, of the planet by radius yield plausible results, while simulations in annuli with larger radial extents produce jets that are too closely spaced.^{14,15}

The rotating shallow water equations are widely used in geophysical and planetary fluid dynamics as conceptual models for rotating stratified fluids. Following the pioneering non-divergent barotropic model of Williams,¹⁷ there

^{a)}emma.warneford@maths.ox.ac.uk

^{b)}dellar@maths.ox.ac.uk

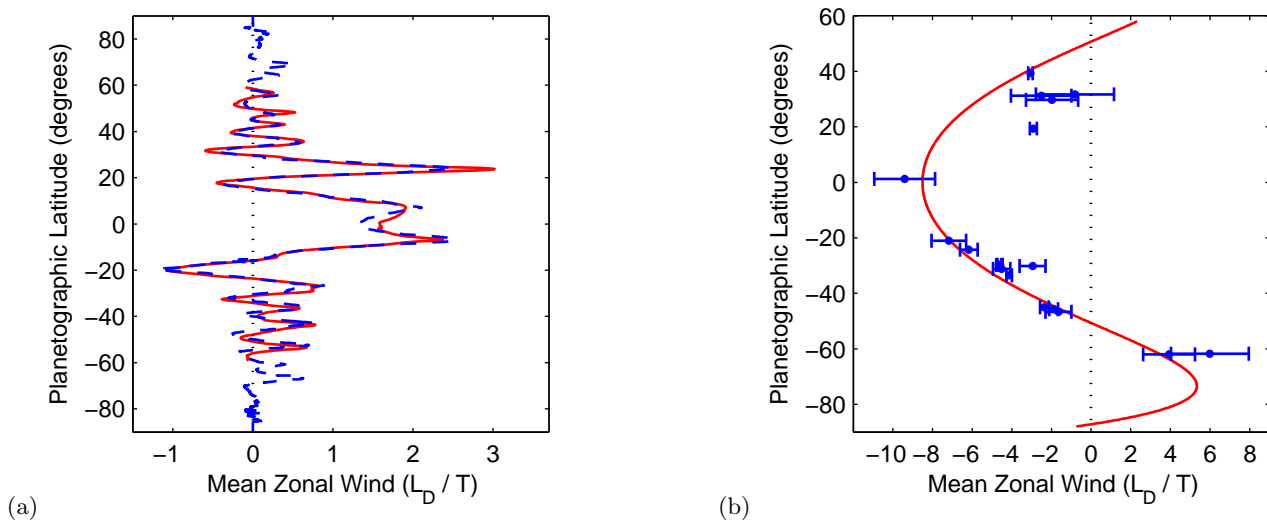


FIG. 1. Mean zonal wind profiles for (a) Jupiter and (b) Neptune, in units of deformation radii per planetary day (L_D/T). Jovian data are from Voyager 2 (solid line)⁴ and Cassini (dashed line).⁵ The Voyager 2 data are restricted to mid and low latitudes. Neptunian data points are from the Hubble Space Telescope.⁶ The solid line is an empirical fit to Voyager 2 data.¹⁶

have been many shallow water studies of the Jovian atmosphere.^{9,18–28} Applications of shallow water theory to the gas giant planets are typically motivated by the two-layer model depicted in Fig. 2, in which a thin weather layer overlies a denser and much deeper layer. In the limit of an infinitely deep and quiescent lower layer, the two-layer system reduces to the shallow water equations for the upper layer, as in (1) below, but with the true gravity g replaced by a reduced gravity g' . This is known as a $1\frac{1}{2}$ -layer, equivalent barotropic, or reduced gravity model.^{18,26,29,30}

Cho and Polvani^{22,23} performed freely decaying simulations of the shallow water equations on a smooth sphere:

$$h_t + \nabla \cdot (h\mathbf{u}) = 0, \quad (1a)$$

$$\mathbf{u}_t + (\mathbf{u} \cdot \nabla) \mathbf{u} + f\hat{\mathbf{z}} \times \mathbf{u} = -g'\nabla h, \quad (1b)$$

where h is the height of the active layer, \mathbf{u} is its depth-averaged horizontal velocity, $\nabla = (\partial_x, \partial_y)^T$ is the horizontal gradient operator, and $\hat{\mathbf{z}}$ is a unit vector in the local vertical direction. The traditional Coriolis parameter is $f = 2\Omega \sin \phi$ at latitude ϕ on a planet rotating with angular velocity Ω . We will refer to these equations as the “standard” shallow water equations, to distinguish them from the other models we introduce below.

Initialized with a random turbulent flow, these freely decaying simulations captured many qualitative features of the gas giant atmospheres.^{22,23} In particular, zonal jets inevitably appear as the turbulent inverse cascade to larger scales is arrested at the Rhines scale through coupling to Rossby waves.^{3,30,31} However, simulations with Jovian parameters produced 10–15 jets instead of the observed 30 jets. These simulations, and subsequent forced-dissipative simulations, invariably produced retrograde jets at the equator when run with Jovian parameter values.^{22–28} Prograde equatorial jets have been found in forced-dissipative simulations with much larger deformation radii, $L_D \gtrsim a$, the planetary radius, with a trend towards retrograde jets as L_D decreases.²⁷ Prograde jets were also found in ensemble studies of freely decaying turbulence at larger Rossby numbers run for relatively short times of up to 119 rotation periods, although the simulations showed a trend towards more retrograde jets after longer times.³²

Scott and Polvani^{27,28} introduced dissipation into the shallow water height equation to produce the model

$$h_t + \nabla \cdot (h\mathbf{u}) = -(h - h_0)/\tau_{\text{rad}}, \quad (2a)$$

$$\mathbf{u}_t + (\mathbf{u} \cdot \nabla) \mathbf{u} + f\hat{\mathbf{z}} \times \mathbf{u} = -g'\nabla h + \mathbf{F}, \quad (2b)$$

where \mathbf{F} is a narrow-band isotropic random forcing of the kind described in Sec. III D. The right hand side of (2a) relaxes h towards a mean layer depth h_0 with time scale τ_{rad} . This relaxation is intended to model heating or cooling by radiation, following earlier models of the terrestrial stratosphere.^{33–35} Simulations with $\tau_{\text{rad}} = (a/L_D)^2 \pi / (2\Omega)$ produced prograde equatorial jets for several different ratios of the deformation radius $L_D = \sqrt{g'h_0}/(2\Omega)$ to the planetary radius a .

If we consider the two-layer model in Fig. 2, the right hand side of (2a) arises from imagining that radiative heating or cooling causes fluid parcels to cross the interface between the upper weather layer and the deep quiescent layer below. Setting aside the question of how well this picture describes the Jovian atmosphere, there is some uncertainty over how the mass exchange across the interface should contribute to the momentum equation. The radiative term in the Scott and Polvani^{27,28} model does not conserve momentum, because (2a) and (2b) together imply

$$(h\mathbf{u})_t + \nabla \cdot (h\mathbf{u}\mathbf{u} + \frac{1}{2}g'h^2\mathbf{I}) + f\hat{\mathbf{z}} \times (h\mathbf{u}) = -(h - h_0)\mathbf{u}/\tau_{\text{rad}}, \quad (3)$$

in the absence of forcing. Shell and Held³⁵ considered the slightly different model

$$h_t + \nabla \cdot (h\mathbf{u}) = -(h - h_0)/\tau_{\text{rad}}, \quad (4a)$$

$$\mathbf{u}_t + (\mathbf{u} \cdot \nabla) \mathbf{u} + f\hat{\mathbf{z}} \times \mathbf{u} = -g'\nabla h + \mathbf{F} + (1 - h_0/h)\mathcal{H}(h - h_0)\mathbf{u}/\tau_{\text{rad}}, \quad (4b)$$

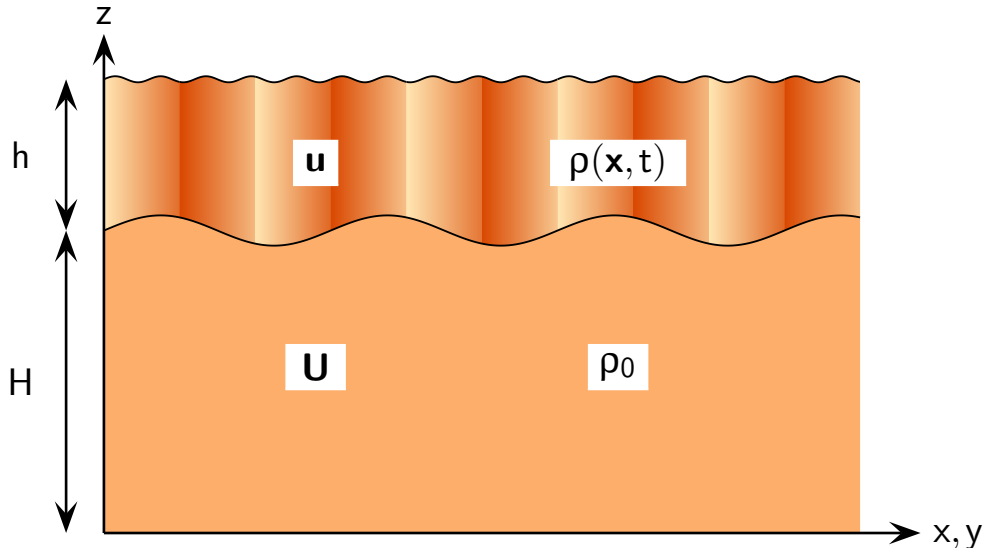


FIG. 2. A stably stratified two-layer system with density $\rho(\mathbf{x}, t) < \rho_0$ in the upper layer. The equivalent barotropic approximation allows the lower layer to be treated as quiescent when $h \ll H$, $|\mathbf{U}| \ll |\mathbf{u}|$, and $\rho_0 - \rho(\mathbf{x}, t) \ll \rho_0$. The standard shallow water equations take ρ to be constant in the upper layer.

where $\mathcal{H}(h - h_0)$ is the Heaviside step function. The asymmetry arises from the expectation that when $h > h_0$ fluid parcels leave the active layer without changing the mean velocity of that layer. Conversely, when $h < h_0$, fluid from the quiescent lower layer enters and mixes with the active layer while conserving total momentum, thus lowering the mean velocity of the active layer.

These difficulties originate from the fixed relation between the layer depth h and the pressure $(1/2)g'h^2$ in the standard shallow water equations. In reality, a warmer column of gas should exert a larger pressure than a cooler column with the same mass. Radiative cooling should affect the difference in temperature, but not the mass. The thermal shallow water equations extend the standard shallow water theory by permitting horizontal variations in the thermodynamic properties of the fluid within each layer. They were introduced by Lavoie³⁶ to describe atmospheric mixed layers over frozen lakes, and later adopted for tropical and coastal oceans, and the upper ocean mixed layer,^{37–41} while their theoretical properties were developed by Ripa.^{42–44} Thermal shallow water theory has close connections with shallow water models of moist convection,^{45,46} and with shallow water magnetohydrodynamics.^{47,48} In this paper we present the thermal shallow water equations as an alternative model for Jovian atmospheres, exploiting the analogy between Jovian cloud decks and the upper ocean mixed layer.

II. THERMAL SHALLOW WATER EQUATIONS

Shallow water theory describes one or more layers of inviscid fluid. The horizontal velocity within each layer is taken to be depth-independent, so the fluid moves in columns. Shallow water theory may be derived from the three-dimensional Euler equations for a Boussinesq fluid by posing asymptotic expansions of the velocity and pressure in a small ratio between vertical and horizontal length scales, followed by depth-averaging across each layer.^{29,30}

Shallow water theory typically arises in a Jovian context under the equivalent barotropic or $1/2$ -layer approximation.^{18,26,29,30} The scenario sketched in Fig. 2 contains two distinct layers of unequal depths separated by a sharp density contrast. The upper layer may be identified with the weather layer, or cloud deck, which extends upwards to negligibly low pressures. The interface between the two layers may be plausibly related to a change in stratification due to a localised release of latent heat from water vapor condensing at the 5 to 10 bar pressure level.^{3,8} The deeper atmosphere may be convective, and thus largely unstratified,^{49,50} but some density contrast must exist to support the internal gravity waves observed propagating outwards from the impact points of Shoemaker–Levy comet debris.^{11,12} The equivalent barotropic approximation gives a closed set of shallow water equations for the upper layer alone when the lower layer is much deeper and relatively quiescent. The effect of the lower layer is to replace the actual gravitational acceleration g by the reduced gravity $g' = g\Delta\rho/\rho_0$, where $\Delta\rho$ is the density contrast between the two layers.

Standard shallow water theory assumes a fixed density contrast $\Delta\rho$. It may be extended by relaxing the homogeneity assumption for the upper layer, which is then characterised by a spatially varying density contrast $\Delta\rho = \rho_0 - \rho(\mathbf{x}, t)$ from the lower layer with constant density ρ_0 . Indeed, horizontal variations in the 5 to 10K temperature contrast mentioned above have been invoked to justify a vertical shear between the observed cloud layer and a convective interior through the thermal-wind relation.^{51,52} We introduce $\Theta = g\Delta\rho/\rho_0$ to represent this density contrast, using a different symbol to emphasise that Θ is a function of \mathbf{x} and t . The equivalent barotropic approximation then leads to

the thermal shallow water equations:

$$h_t + \nabla \cdot (h\mathbf{u}) = 0, \quad (5a)$$

$$\Theta_t + (\mathbf{u} \cdot \nabla) \Theta = -(\Theta h/h_0 - \Theta_0)/\tau_{\text{rad}}, \quad (5b)$$

$$\mathbf{u}_t + (\mathbf{u} \cdot \nabla) \mathbf{u} + f\hat{\mathbf{z}} \times \mathbf{u} = -\nabla(\Theta h) + \frac{1}{2}h\nabla\Theta. \quad (5c)$$

The momentum equation (5c) reduces to the standard shallow water momentum equation for a homogeneous layer when Θ is constant. We have added a Newtonian cooling term $-(\Theta h/h_0 - \Theta_0)/\tau_{\text{rad}}$ on the right hand side of (5b). This represents radiative relaxation towards a temperature $\Theta_0 h_0/h$ with time scale τ_{rad} . The h -dependence represents the idea that columns that extend higher are able to radiate more effectively. In this respect, one should think of the upper layer extending upwards indefinitely with an exponentially decaying density, rather than terminating at a sharp upper boundary as in the terrestrial oceanic context more applicable to Fig. 2.

Our thermal shallow water model conserves both mass and momentum within the active layer,

$$(h\mathbf{u})_t + \nabla \cdot (h\mathbf{u}\mathbf{u} + \frac{1}{2}\Theta h^2\mathbf{I}) + f\hat{\mathbf{z}} \times (h\mathbf{u}) = 0, \quad (6)$$

because we include the radiative relaxation term in a separate temperature equation, not in the continuity equation. The Coriolis force may be incorporated into the time derivative and divergence terms by introducing a vector potential for the Coriolis parameter, as described in Sec. VI. The thermal shallow water equations imply the evolution equation

$$q_t + (\mathbf{u} \cdot \nabla) q = \hat{\mathbf{z}} \cdot (\nabla h \times \nabla \Theta)/(2h) \quad (7)$$

for the standard shallow water potential vorticity $q = (f + v_x - u_y)/h$. The potential vorticity is not materially conserved following individual fluid elements, as it is under the standard shallow water equations, but instead the total potential vorticity inside each closed Θ -contour is conserved.⁴⁸ The source term on the right hand side of (7) is the depth average of the baroclinic torque in a continuously stratified fluid,^{44,53} and the conservation of potential vorticity inside closed isotherms is analogous with the potential vorticity impermeability property of isentropic surfaces in three dimensions.³⁰

We presented two derivations of the thermal shallow water equations in Ref. 53. The first derivation rescales the three-dimensional Boussinesq equations for the upper layer in Fig. 2 with a small aspect ratio between vertical and horizontal length scales, followed by depth-averaging and the application of the equivalent barotropic approximation. The second derivation projects the three-dimensional Lagrangian for a Boussinesq fluid onto columnar fluid motions,⁵⁴ and then applies Hamilton's principle. There is a close parallel between the thermal shallow water equations and shallow water models of moist convection,^{45,46} with Young's depth-averaged description of the upper oceanic mixed layer,⁵⁵ and with the shallow water magnetohydrodynamic equations.^{47,48} Horizontal gradients in Θ create depth-dependent horizontal gradients of the hydrostatic pressure, which are absent in standard shallow water theory. The assumption that the fluid continues to move in columns thus requires vertical mixing of horizontal momentum, as included explicitly in Young's model of the oceanic mixed layer,⁵⁵ and as provided by the convection associated with cloud decks in terrestrial and Jovian atmospheres.^{8,29,56,57}

These shallow models require just a few parameters: the planetary radius a , rotation period $T = 2\pi/\Omega$, gravity wave speed $\sqrt{\Theta_0 h_0}$, and the radiative relaxation rate. The first two are easily determined from observations, and we have a good knowledge of the internal gravity wave speed on Jupiter from observing waves propagating outwards from the impacts of Shoemaker–Levy comet debris.^{11,12} These and other data from Refs. 9 and 13 are given in Table I. We use the radiative relaxation time scale formula from Houghton⁵⁷

$$\tau_{\text{rad}} = \frac{c_p p}{8\sigma g \mathcal{T}^3}, \quad (8)$$

where \mathcal{T} and p are the gas temperature and pressure respectively, $\sigma = 5.670 \times 10^{-8} \text{J m}^{-2} \text{s}^{-1} \text{K}^{-4}$ is the Stefan–Boltzmann constant, and $c_p = 1.26 \times 10^4 \text{J kg}^{-1} \text{K}^{-1}$ is the specific heat for a hydrogen atmosphere in the Jovian temperature range.¹⁵

Liu and Schneider¹⁵ compared three-dimensional general circulation model (GCM) simulations with observations at the 25 millibar pressure level for Neptune. We used this pressure level to calculate radiative relaxation time scales for both Jupiter and Neptune. For Jupiter, we consider a cloud layer that extends downwards on the order of 100 km from the 25 millibar pressure level, as suggested by observations of moist convection.⁵⁶ The latent heat released by condensation of water vapor suggests a temperature contrast of around $\Delta\mathcal{T} = 10\text{K}$, giving a reduced gravity $\Theta_0 = g\Delta\mathcal{T}/\mathcal{T} \approx 2 \text{m s}^{-2}$. This requires a layer depth $h_0 \approx 200 \text{km}$ to match the observed internal wave speed. At the 25 millibar level, $\mathcal{T} \approx 120 \text{K}$ for Jupiter,⁵⁸ giving a radiative relaxation time scale of 429 hours, or 43 Jovian days. Neptune has a much lower temperature at the 25 millibar level, $\mathcal{T} \approx 60 \text{K}$,¹³ which gives a slightly lower specific heat capacity $c_p = 1.12 \times 10^4 \text{J kg}^{-1} \text{K}^{-1}$, and has a lower gravity, $g = 11.2 \text{m s}^{-2}$.¹⁵ Together these differences give a much longer radiative time scale of 7088 hours, or 396 Neptunian days. These and other parameter values for Jupiter and Neptune are summarised in Table I.

TABLE I. Parameter values for Jupiter and Neptune^{9,13}

	a (10^7 m)	$2\pi/\Omega$ (hours)	$\sqrt{\Theta_0 h_0}$ (m s^{-1})	g (m s^{-2})	\mathcal{T} (K)	τ_{rad} (hours)
Jupiter	7.1	9.9	678	26	120	429
Neptune	2.5	17.9	574	11.2	60	7088

III. NUMERICAL FORMULATION

A. Dimensionless equations

We non-dimensionalize our various shallow water models using the deformation radius $L_D = \sqrt{\Theta_0 h_0}/(2\Omega)$ and the planetary rotation period $T = 2\pi/\Omega$ as length and time scales. We scale h and Θ with their equilibrium values h_0 and Θ_0 , and take $g' = \Theta_0$ for the non-thermal models. The dimensionless height-damped shallow water model is then defined by

$$h_t + \nabla \cdot (h\mathbf{u}) = -\lambda(h - 1), \quad (9a)$$

$$\mathbf{u}_t + (\mathbf{u} \cdot \nabla) \mathbf{u} + \frac{1}{\text{Ro}} f \hat{\mathbf{z}} \times \mathbf{u} = -\frac{1}{\text{Ro}^2} \nabla h + \mathbf{F} - \alpha \mathbf{u}. \quad (9b)$$

We have a fixed nominal Rossby number $\text{Ro} = 1/(4\pi)$ due to our velocity scale being $U = L_D/T = L_D\Omega/(2\pi)$. The true Rossby numbers calculated from the root-mean-square (RMS) velocities in our simulations will be within 20% of this value, as described below. No Burger number appears because we have scaled horizontal lengths with the deformation radius L_D . The dimensionless radiative relaxation rate is λ . We have added a forcing \mathbf{F} , as described below, and a linear drag with rate α to dissipate energy at the largest scales. These scales would otherwise grow secularly due to the slow leakage of energy past the Rhines scale in the inverse cascade, and would thus prevent a Jovian-like banded structure from persisting as a statistical steady state.³

The standard shallow water model sets $\lambda = 0$. A variant that conserves momentum during radiative relaxation may be written as

$$h_t + \nabla \cdot (h\mathbf{u}) = -\lambda(h - 1), \quad (10a)$$

$$\mathbf{u}_t + (\mathbf{u} \cdot \nabla) \mathbf{u} + \frac{1}{\text{Ro}} f \hat{\mathbf{z}} \times \mathbf{u} = -\frac{1}{\text{Ro}^2} \nabla h + \lambda(1 - 1/h) \mathbf{u} + \mathbf{F} - \alpha \mathbf{u}, \quad (10b)$$

where we have omitted the Heaviside step function from the Shell and Held model.³⁵ We call this model the momentum-conserving model, and collectively call (9) and (10) the two height-damped models. The dimensionless thermal shallow water model is

$$h_t + \nabla \cdot (h\mathbf{u}) = 0, \quad (11a)$$

$$\Theta_t + (\mathbf{u} \cdot \nabla) \Theta = -\lambda(h\Theta - 1), \quad (11b)$$

$$\mathbf{u}_t + (\mathbf{u} \cdot \nabla) \mathbf{u} + \frac{1}{\text{Ro}} f \hat{\mathbf{z}} \times \mathbf{u} = -\frac{1}{\text{Ro}^2} (\nabla(\Theta h) - \frac{1}{2} h \nabla \Theta) + \mathbf{F} - \alpha \mathbf{u}. \quad (11c)$$

We later call this the thermal model for brevity. The control parameters are thus the domain size, in units of deformation radii, the radiative damping rate λ , the frictional damping rate α , and the properties of the forcing \mathbf{F} . Values of these parameters for Jupiter and Neptune are given in Table II.

B. Square planet domain

The self-organisation of geostrophic turbulence into zonal jets takes place over many eddy turnover times. Cho and Polvani²² showed that some early simulations^{17,59,60} of non-divergent flows were not integrated for long enough to reach statistically steady states. We simulated all four models using graphical processing units (GPUs) that offer high memory bandwidth and floating point performance for many scientific algorithms, with performance characteristics resembling the vector machines widely used to simulate atmospheric flows in the 1990s. However, spherical harmonic transform implementations for GPUs are only beginning to appear, and their performance remains comparable with conventional microprocessors.⁶¹

Instead, we solve our equations in the doubly-periodic Cartesian domain sketched in Fig. 3, which we refer to as the square planet domain. The horizontal x coordinate denotes longitude, while the vertical y axis denotes latitude. We take our dimensionless Coriolis parameter to be the periodic function $f(y) = \cos(2\pi y/y_{\text{max}})$, where y_{max} is the dimensionless side length of our domain. Starting from the north pole at the top of the domain, and decreasing y , we reach the equator a quarter of the way down, and the south pole half way down. We then continue to reach the equator again, before returning to the north pole, now at the bottom of the domain. In other words, we imagine following a meridian (constant longitude line) from the north pole to the equator to the south pole, and then following a second meridian with longitude offset by 180° back across the equator to the north pole. This domain lets us use

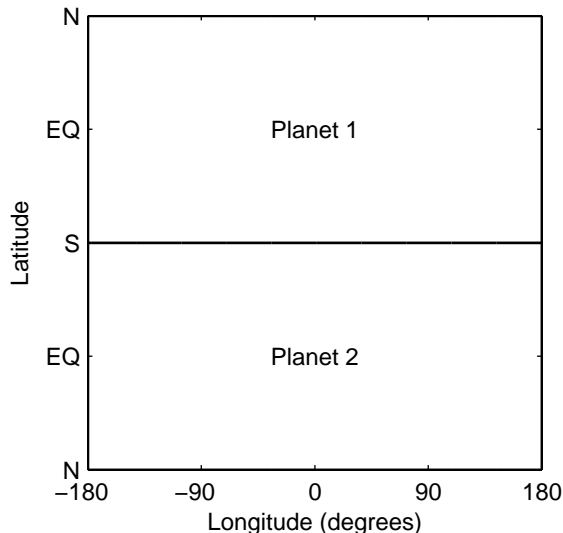


FIG. 3. Schematic of the domain in which we solve our equations. The x axis denotes the full range of longitude, and the y axis denotes latitude (where starting at the top of the y axis and moving down we have the north pole, then the equator, then the south pole, then back to the equator, and finally back to the north pole). Each half of the domain denotes a full copy of the planet. For clarity, we plot our simulation results for only the top planet (planet 1).

Fourier spectral methods based on the GPU fast Fourier transform implementation. The poles do not consist of a single point in this domain, but each is a line in longitude (although the north pole horizontal lines at the bottom and top of the square planet domain will be the same due to the periodic boundary condition). Our results in Sec. IV are in good qualitative agreement with spherical simulations,^{22,23,27,28} and our zonal energy spectra $E(k_y)$ are consistent with observations of Jupiter (see Sec. V) although we expect some distortion at high latitudes. Each half of the domain corresponds to a complete planet, so we plot our simulation results for only the upper planet (planet 1 in Fig. 3).

C. Numerical method

The four dimensionless models were discretized in space using a grid of 1024×1024 Fourier collocation points, with the nonlinear terms being computed pseudo-spectrally. We integrated the resulting large system of ordinary differential equations using the standard fourth-order Runge–Kutta scheme, with a time step determined dynamically from the Courant–Friedrichs–Lewy condition $\sqrt{2}k_{\max}c_{\max}\Delta t < 2.4$, a slightly reduced threshold, with $k_{\max} = 1024\pi/y_{\max}$ the maximum resolved horizontal wavenumber for our domain. The dimensionless maximum wave speed is $c_{\max} = \max(\sqrt{\Theta h}/\text{Ro} + |\mathbf{u}|)$ for the thermal shallow water equations, and $c_{\max} = \max(\sqrt{h}/\text{Ro} + |\mathbf{u}|)$ for the other three models. The maxima are taken over all grid points in the domain. To prevent the build-up of enstrophy at the highest resolved wavenumbers, we used the tensor product form of the one-dimensional Hou–Li spectral filter that multiplies the Fourier coefficient with wave vector (k_x, k_y) by $\exp\{-36[(k_x/k_{\max})^{36} + (k_y/k_{\max})^{36}]\}$ after each Runge–Kutta timestep.⁶² The energy spectra shown in Sec. V confirm that this filter provides sufficient dissipation at the finest resolved scales without the parameter adjustment required by more conventional hyperviscous dissipation.

D. Forcing

We took $h = 1$ and $u = v = 0$ as initial conditions for all four models, and $\Theta = 1$ for the thermal model. We drove the turbulence by applying a divergence-free isotropic random forcing to \mathbf{u} . We forced inside a narrow annulus of wavenumbers $|\mathbf{k}| \in [k_c - 2, k_c + 2]$ centered around a wavenumber k_c . These wavenumbers are counted from the longest sinusoidal mode in the domain being wavenumber 1. We forced each mode with amplitude ϵ_f using random phases that are δ -correlated (white) in time. This type of forcing corresponds to the zero-correlation-time limit of the forcing introduced by Lilly.⁶³ It has been widely used in numerical studies of zonal jet formation,^{27,64–66} and may be interpreted as a model for small-scale three-dimensional convection. Three-dimensional geostrophic turbulence theory suggests an injection of energy into the lowest vertical mode at horizontal lengthscales comparable to the deformation radius.⁶⁷ We followed Scott and Polvani^{27,28} in taking $k_c = 42$ for our Jovian simulations in Sec. IV. Setting $k_c = k_{\max}/4$ leaves sufficiently many larger wavenumbers for a forward enstrophy cascade,⁶⁸ and gives $k_c = 42$ for the T170 spherical harmonic truncation used in their lower resolution simulations.²⁷ This value for k_c is consistent with analyses of energy spectra reconstructed from Cassini observations of Jupiter that suggest that the break in the spectral slope indicative of the forcing scale lies at wavenumbers somewhat below 100.⁶⁹

There is no analytical theory for the energetics of forcing combined with radiative cooling, as there is for Rayleigh

TABLE II. Dimensionless parameter values for Jupiter and Neptune

	$y_{\max} = 2\pi a/L_D$	$\lambda^{-1} = \tau_{\text{rad}}/T$	$\mathcal{E}_{\infty}/y_{\max}^2$	k_c	α^{-1}
Jupiter	232	43	0.37	42	10^3
Neptune	53	396	0.71	10	10^3

friction alone.²⁷ Instead, we adjusted the forcing amplitude ϵ_f at each time step so that the kinetic energy roughly followed the prescribed profile $\mathcal{E}(t) = \mathcal{E}_{\infty} \tanh(t/t_{\text{ramp}})$ with $t_{\text{ramp}} = 1000$ planetary days. If the kinetic energy exceeded $\mathcal{E}(t)$ at the start of the time step, we decreased the forcing strength ϵ_f by a factor of $\exp(-\Delta t/t_{\text{adj}})$. If instead the kinetic energy was less than $\mathcal{E}(t)$, we increased ϵ_f by a factor of $\exp(\Delta t/t_{\text{adj}})$. We took $t_{\text{adj}} = 50$ planetary days in all cases. Setting $\mathcal{E}_{\infty} = 2 \times 10^4$, or about 0.37 per unit area, gives zonal jet speeds comparable to those shown in Fig. 1(a) for Jupiter. Using \mathcal{E}_{∞} to determine a velocity scale $u_{\text{RMS}} \approx 0.86 L_D/T$ leads to our Jovian simulations having Rossby number $u_{\text{RMS}}/(2\Omega L_D) \approx 0.069$ in their eventual statistical steady states.

This method of forcing enables us to draw fair comparisons between solutions of the four models, each with the same kinetic energy. In controlling the kinetic energy rather than the total energy, we follow the “thermostatting” approach widely used to control the kinetic energy in molecular dynamics simulations.⁷⁰ If we used a constant forcing strength throughout, it would be very difficult to determine values of ϵ_f to give comparable kinetic energies in the four different models. We also used the calculated average of the forcing strength from a self-adjusting simulation that had reached a statistical steady state to provide a value of ϵ_f for a second run with constant forcing amplitude. The two solutions were very similar.

We used the MT19937 variant of the Mersenne Twister algorithm⁷¹ to generate uniformly distributed random phases. We present detailed simulation results for one particular value of the seed, but simulations with a different initial seed gave very similar results, as quantified by the error indicators on the diagnostics in Table III, as did simulations with the Mersenne Twister replaced by the ACORN random number generator.⁷² In both cases we executed the generator on the host microprocessor, and copied the resulting sequence of random numbers to the GPU. A simple linear congruential generator running directly on the GPU produced noticeably different results from these two much more sophisticated generators.

E. Performance

The fast Fourier transforms accounted for 66% of the computational time in our GPU code, which performed about 22 timesteps per second at 1024×1024 resolution. Most of the rest of the time was taken up with computing the nonlinear terms. Each calculation of the four time derivatives of h, u, v, Θ required sixteen fast Fourier transformations of single fields. These together took 7.4 milliseconds on an Nvidia K20c GPU, and 38 milliseconds using FFTW 3.2.2 with 8 threads (the optimal number) across two Intel E5-2640 CPUs. This is a factor of five speed-up. Even assuming the rest of the CPU code took no time, our GPU code would be 3.5 times faster. This is consistent with our GPU code being about 24 times faster than our original single-threaded CPU code.

IV. JOVIAN SIMULATIONS

Figure 4 shows the instantaneous relative vorticity $\omega = \hat{\mathbf{z}} \cdot \nabla \times \mathbf{u}$ after 2×10^4 Jovian days for the four different shallow water models. Figure 5 shows the corresponding zonal velocity and temperature fields for the thermal shallow water model. We show only the top half of the domain, planet 1 in Fig. 3, for ease of interpretation. All four simulations show a mixture of vortices and zonally elongated structures. The temperature fluctuations in the northern hemisphere of Fig. 5(a) have a correlation coefficient of 0.29 with respect to the relative vorticity shown in Fig. 4(d). Cyclonic regions are thus typically warmer than anticyclonic regions, in agreement with Jovian observations.³

Figure 6 shows the corresponding instantaneous zonally-averaged zonal velocity, $\bar{u} = y_{\max}^{-1} \int u(x, y, t) dx$, in units of deformation radii per Jovian day. The standard shallow water model shows a strong retrograde equatorial jet, as found in previous simulations using Jovian parameters,^{3,22–28} while the other three models show strong prograde equatorial jets. The two height-damped models produce only very weak jets away from the equator. The thermal model shows stronger jets at around 40° either side of the equator, while the standard shallow water model shows two pairs of even stronger jets of roughly equal magnitudes at 20° and 45° either side of the equator. We quantify this difference by calculating the kurtosis, or flatness, of the pointwise zonal velocity field,

$$\mathcal{K}_u(t) = \langle u^4 \rangle / \langle u^2 \rangle^2, \quad (12)$$

where $\langle \cdot \rangle$ denotes an average over the entire simulation domain (planets 1 and 2). Figure 7(a) shows that the kurtosis begins near three, as for a Gaussian random variable, in each simulation. It increases due to the formation of coherent structures (such as zonal jets), and finally levels off as the flow reaches a statistical steady state. The two height-damped models produce zonal velocity fields with a kurtosis that is roughly twice as large as for the other two models. While the kurtosis also includes contributions from vortices and filaments, these much larger kurtosis values primarily reflect the dominance of the equatorial jets in the two height-damped models. Although subject to more statistical

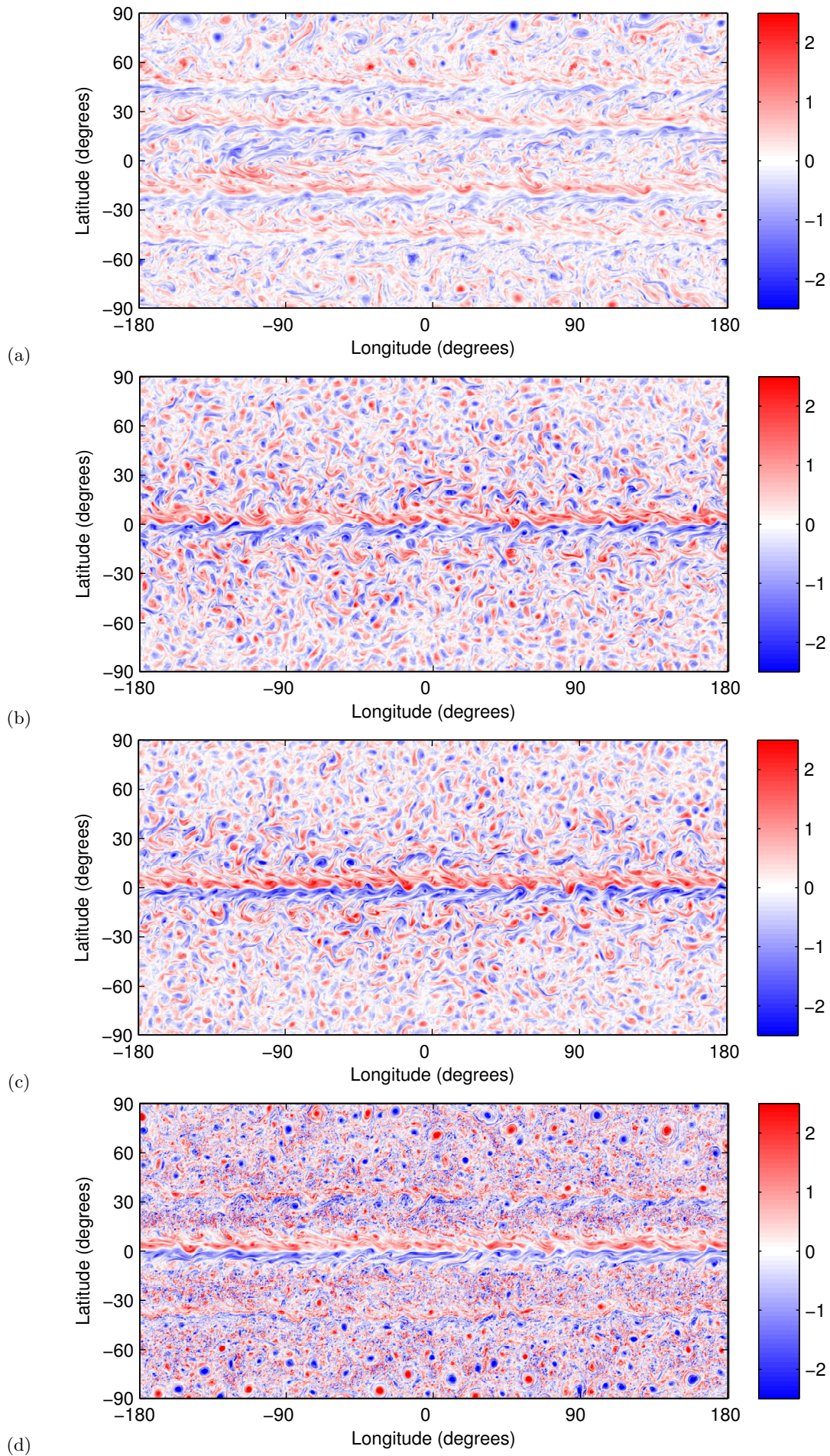


FIG. 4. Dimensionless relative vorticity after 2×10^4 Jovian days for the four shallow water models: (a) standard shallow water, (b) height-damped, (c) momentum-conserving height-damped, (d) thermal. Extreme values have been truncated outside the ranges shown on the color bars to show structure at intermediate values more clearly.

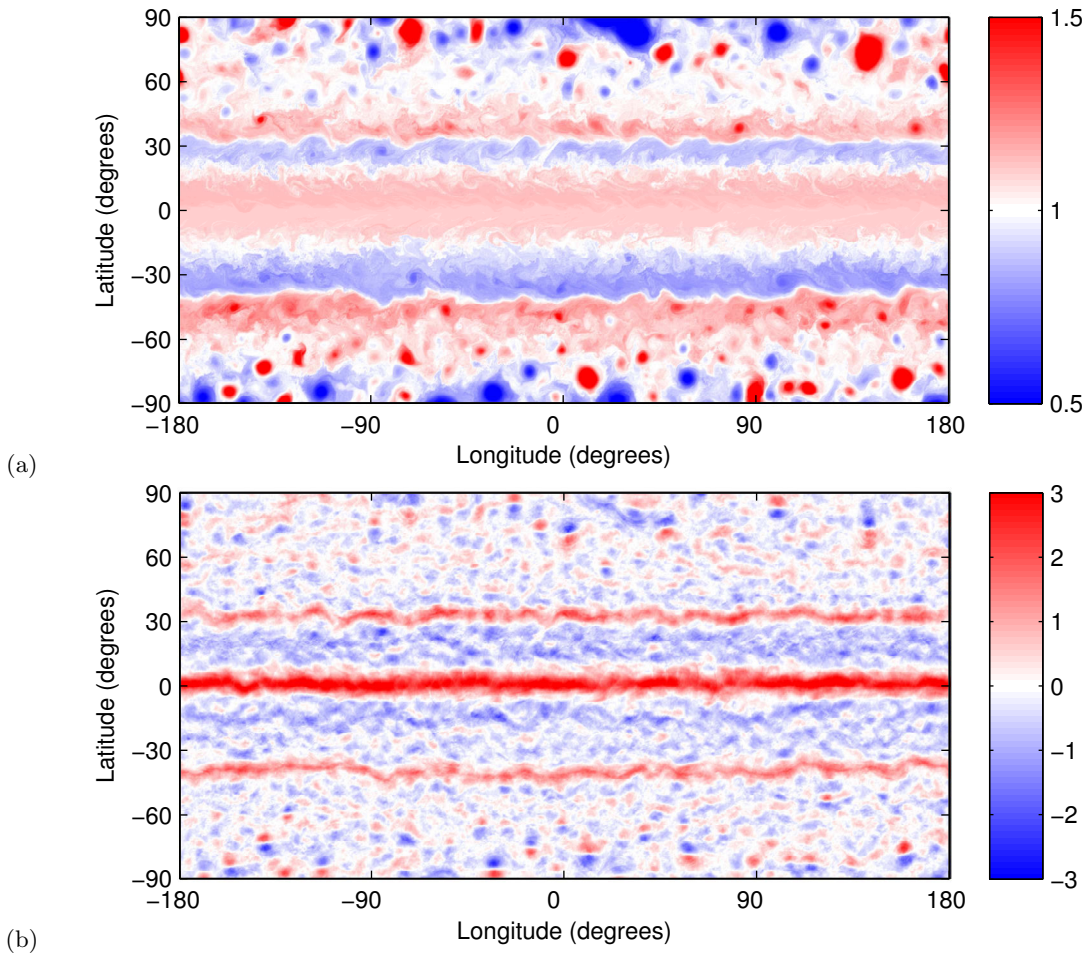


FIG. 5. Dimensionless (a) temperature, and (b) zonal velocity from the thermal shallow water simulation after 2×10^4 Jovian days. Extreme values have been truncated outside the ranges shown on the color bars to show structure at intermediate values more clearly.

noise during simulations, the kurtosis of the zonal average \bar{u} is also noticeably much larger in the two height-damped simulations. After 2×10^4 Jovian days, $\mathcal{K}_{\bar{u}} = 2.54$ for the standard shallow water model, $\mathcal{K}_{\bar{u}} = 19.69$ for the height-damped model, $\mathcal{K}_{\bar{u}} = 20.34$ for the momentum-conserving height-damped model, and $\mathcal{K}_{\bar{u}} = 10.54$ for the thermal model.

The two height-damped models produce remarkably similar results, in the relative vorticity fields shown in Fig. 4(b,c), the mean zonal velocities shown in Fig. 6(b,c), and in the statistics shown in Table III. This similarity arises because the difference between the two models reduces to an $O(\text{Ro}^2)$ correction to geostrophic balance in the f -plane quasi-geostrophic scaling (see the Appendix). The quasi-geostrophic limits of both models are thus identical, and their common potential vorticity evolution equation contains a hypoviscous dissipation proportional to ψ .²⁷ The coefficient of this dissipation is proportional to f^2 , so it becomes ineffective at low latitudes. This may explain why these models produce a strong equatorial jet, with comparatively little activity at mid and high latitudes compared with the standard or thermal shallow water models. Radiative damping of the height equation thus reproduces a feature of the Rayleigh friction confined to latitudes outside 16° from the equator in three-dimensional simulations by Schneider and Liu.^{15,73} This friction models the magnetohydrodynamic drag experienced by Taylor columns that extend into the electrically conducting inner region at depths below 96% of Jupiter's radius, corresponding to pressures above 10^5 bar. Taylor columns near the equator cross into the other hemisphere without penetrating the deep interior, and so experience no drag in this model.

Table III shows a number of averaged diagnostic quantities computed from the simulations, with $\langle\langle \cdot \rangle\rangle$ denoting the time-average of a quantity over the period between 2×10^4 and 2.18×10^4 Jovian days. For example, $\langle\langle \mathcal{K}_{\bar{u}} \rangle\rangle$ is the time-average of the kurtosis of the zonal velocity, the quantity whose time series is shown in Fig. 7(a). We ran two sets of simulations with different initial random seeds, and we present the mean and half differences to give an indication of the repeatability of the different diagnostics.

All four models produce jet speeds comparable to the Jovian observations shown in Fig. 1(a). The forcing strengths for the four simulations were adjusted by the algorithm described in Sec. IIID to give the same statistically steady kinetic energy $0.37 (L_D/T)^2$ per unit area. Figure 7(b) shows the fraction of the kinetic energy in the zonally-averaged flow, as given by

$$\xi(t) = \langle \bar{h} \bar{u}^2 \rangle / \langle h (u^2 + v^2) \rangle, \quad (13)$$

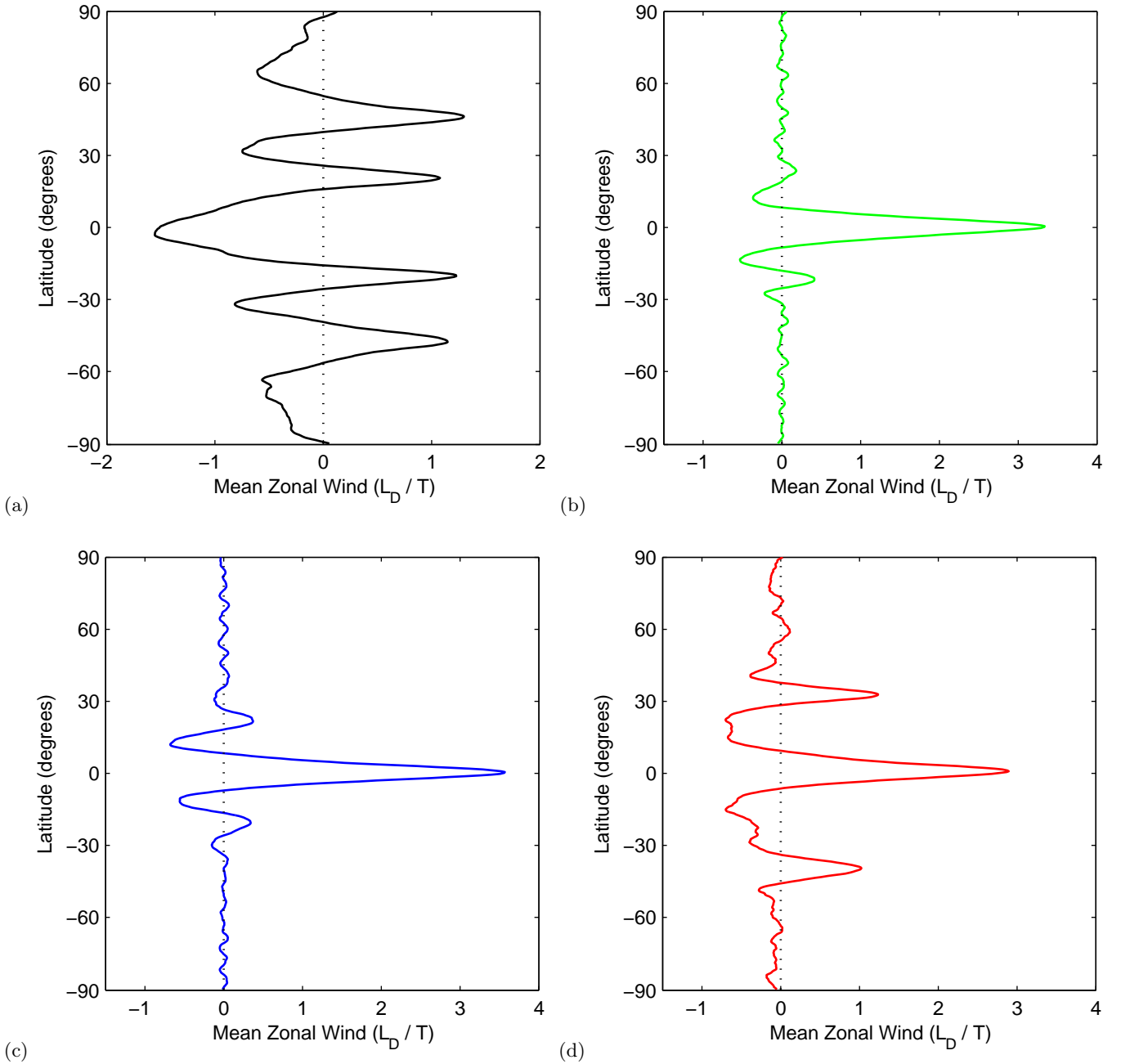


FIG. 6. Mean zonal wind against latitude after 2×10^4 Jovian days for the four shallow water models: (a) standard shallow water, (b) height-damped, (c) momentum-conserving height-damped, (d) thermal.

TABLE III. Average diagnostic quantities in the statistically steady state for two sets of the simulations in Sec. IV with different random seeds. The error estimates quantify the differences between the diagnostics for each pair of simulations.

	$\langle\langle\epsilon_f\rangle\rangle$	$\langle\langle\xi\rangle\rangle$	$\langle\langle\omega_N\rangle\rangle$	$\langle\langle\mathcal{K}_u\rangle\rangle$	$\langle\langle\mathcal{K}_\omega\rangle\rangle$	$\langle\langle\mathcal{S}_\omega\rangle\rangle$
Standard	1300 ± 7	0.58 ± 0.001	-0.023 ± 0.0013	4.05 ± 0.03	3.53 ± 0.027	-0.033 ± 0.019
Height-damped	2900 ± 3	0.51 ± 0.002	0.059 ± 0.0005	12.17 ± 0.09	3.64 ± 0.003	-0.0014 ± 0.004
Momentum-conserving	2800 ± 1	0.54 ± 0.0007	0.062 ± 0.0004	13.03 ± 0.07	3.73 ± 0.009	0.0007 ± 0.0009
Thermal	2200 ± 21	0.49 ± 0.006	0.046 ± 0.0007	6.43 ± 0.08	4.59 ± 0.0008	-0.053 ± 0.022

where \bar{h} and \bar{u} are the zonal means of h and u . The corresponding averages $\langle\langle\xi\rangle\rangle$ are shown in Table III. The zonal mean flow accounts for roughly half the kinetic energy in the three radiatively damped models, and a slightly larger fraction $\langle\langle\xi\rangle\rangle = 0.58$ in the standard shallow water model. All four models produce zonal velocities in the Jovian parameter regime when forced with an amplitude determined by the same desired total kinetic energy. Another such diagnostic is the average forcing amplitude $\langle\langle\epsilon_f\rangle\rangle$, which shows that the three simulations with some form of radiative damping required a forcing amplitude roughly twice as large as that for the standard shallow water model.

Figure 8(a) shows histograms of the relative vorticity in the northern hemisphere of planet 1 after 2×10^4 Jovian days for the four shallow water models. These histograms approximate the relative vorticity probability density functions

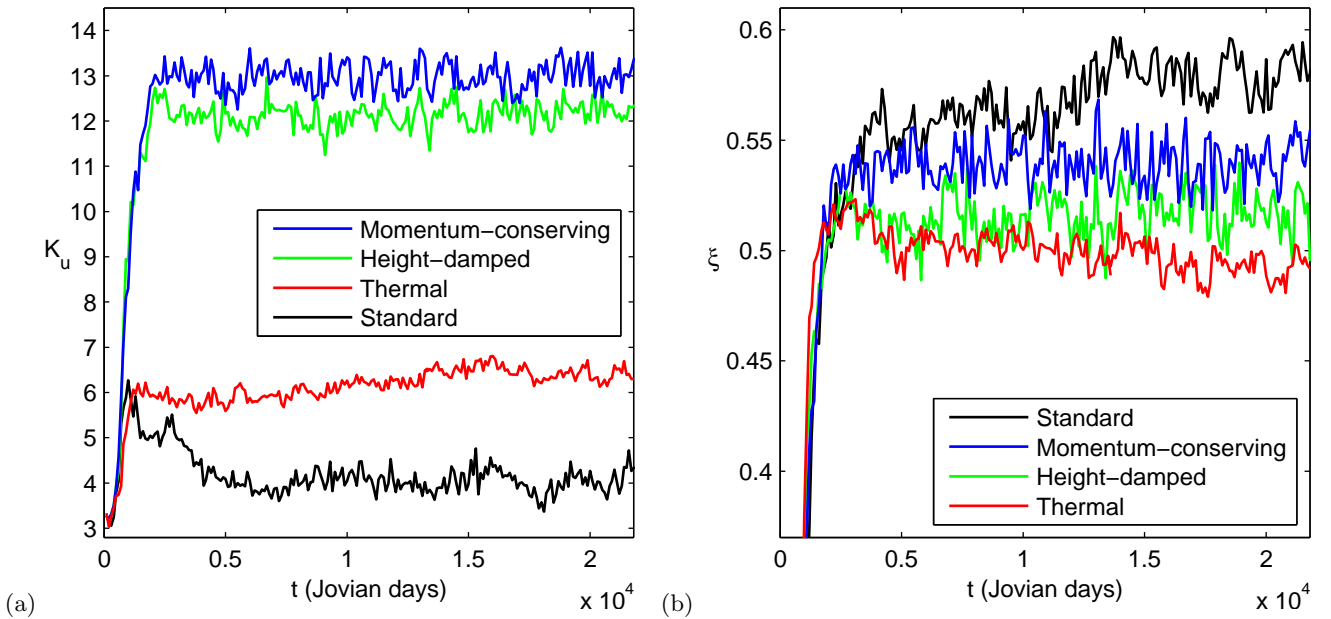


FIG. 7. (a) Evolution of the kurtosis of the zonal velocity. (b) Evolution of the fraction of kinetic energy in the zonally-averaged flow. The four curves in each plot appear in the same top to bottom order as in the legend for that plot.

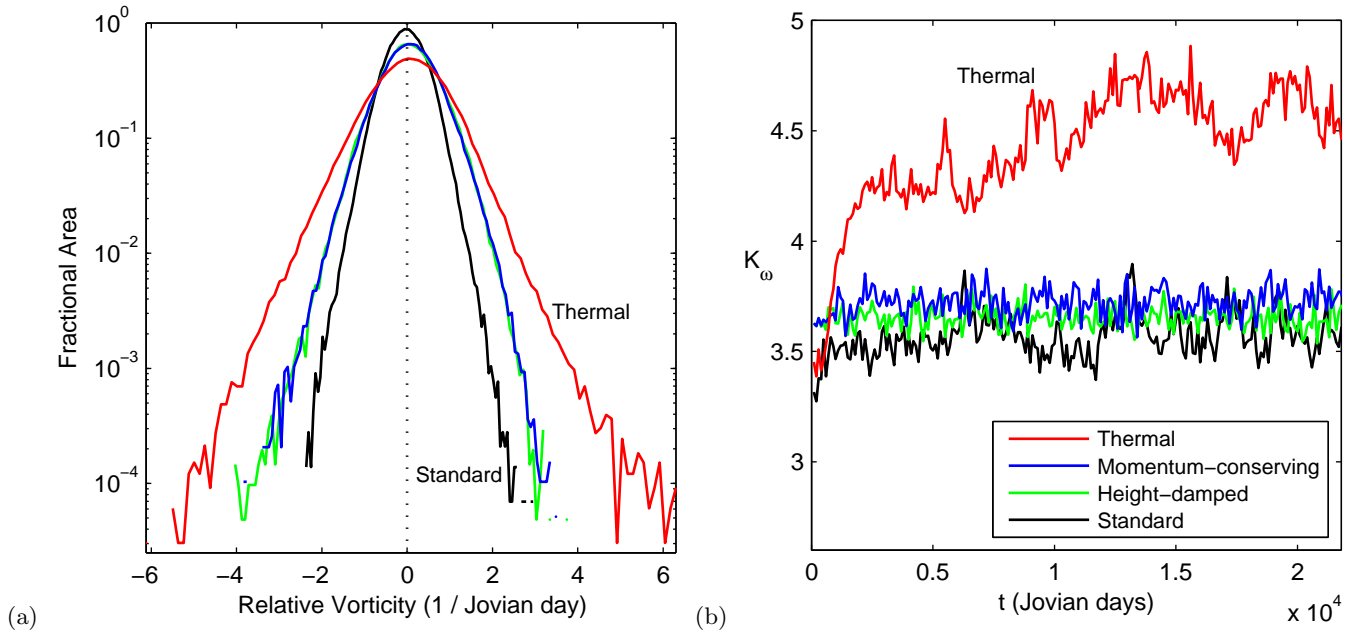


FIG. 8. Panel (a) shows the histogram of the dimensionless relative vorticity at 2×10^4 Jovian days. Panel (b) shows the evolution of the kurtosis of the dimensionless relative vorticity. The four curves in each plot appear in the same top to bottom order as in the legend for that plot

that would arise from an ensemble of simulations with different random seeds. Any breaks in the histograms are due to particular bins having no entries. The tails of the histogram for the thermal shallow water model extend further out than for the other models, demonstrating that this model attains more extreme values for the relative vorticity. The peak of the histogram for the thermal shallow water model is correspondingly lower and broader than for the other three models.

We quantified this difference between the thermal model and the other three models by computing the kurtosis of the relative vorticity field^{74,75}

$$\mathcal{K}_\omega(t) = \langle \omega^4 \rangle / \langle \omega^2 \rangle^2, \quad (14)$$

where $\langle \cdot \rangle$ again denotes an average over the entire simulation domain. The kurtosis of the relative vorticity field is a measure of intermittency, and hence of the formation of coherent structures. A spatially uniform field has a kurtosis of one, whereas a Gaussian random variable has a kurtosis of three. Figure 8(b) shows the evolution of the kurtosis of relative vorticity for all four simulations. The kurtosis for the three non-thermal simulations reaches a statistically steady state by around 1000 Jovian days, and then fluctuates between 3.4 and 3.8. By contrast, the kurtosis for the thermal shallow water model continues to grow for over 10^4 Jovian days, and show subsequent slow oscillations over

thousands of days around a mean of about 4.6. This difference from the other models quantifies the broader tails of the approximate probability distribution function for the vorticity field in the thermal shallow water simulation, as shown in Fig. 8(a).

Shallow water theory is distinguished from quasi-geostrophic theory by an asymmetry between cyclonic and anti-cyclonic relative vorticity.^{27,76} We evaluate this asymmetry for our four different models by plotting the evolution of the mean relative vorticity $\langle \omega \rangle_N$ over the northern hemisphere of planet 1 in Fig. 9(a). The time-average $\langle \langle \omega \rangle_N \rangle$ is shown in Table III. The standard shallow water equations produce a net anticyclonic vorticity, while the other three models all produce a net cyclonic vorticity.

The direction of the equatorial jet is linked to the sign of the mean vorticity in the northern hemisphere.^{25,30} Applying Stokes' theorem to the northern hemisphere of planet 1 gives

$$\iint \omega \, dx dy = \int_E u \, dx + \int_N u \, dx, \quad (15)$$

where the integral on the left is an area integral over the northern hemisphere of planet 1, and the integrals on the right are line integrals around the equator and northern boundary respectively. We have used the periodicity of the domain to cancel the left and right boundary integrals. The last integral would vanish on a sphere, for which the north pole is a point. The last integral is much smaller than the integral around the equator in our simulations since \bar{u} at the northernmost points of the domain is much smaller than \bar{u} at the equator (see Fig. 6). A northern hemisphere with net anticyclonic vorticity must thus exhibit a negative \bar{u} at the equator, and hence a retrograde equatorial jet, while net cyclonic vorticity implies a prograde jet. This consistency relation holds for all four of our models.

The cyclone/anticyclone asymmetry also applies to individual coherent structures.⁷⁶ Voyager and Cassini images show that 90% of the stable, long-lived, compact oval-shaped spots in Jupiter's atmosphere are anticyclonic.^{77,78} Cyclonic vorticity tends to occur in filamentary regions, rather than compact oval-shaped spots.^{3,77,78} We quantify this asymmetry using the skewness of the relative vorticity field,^{25,27}

$$S_\omega(t) = \langle (\omega - \langle \omega \rangle_N)^3 \rangle_N / \langle (\omega - \langle \omega \rangle_N)^2 \rangle_N^{3/2}, \quad (16)$$

where $\langle \cdot \rangle_N$ denotes the average of the quantity inside the angle brackets over the northern hemisphere of planet 1. Figure 9(b) shows the evolution of the skewness of the relative vorticity for the four different models. The skewnesses in all four models are close to zero. The skewnesses of the two height-damped models oscillate around zero, while the skewnesses of the standard and thermal models are more robustly negative. The latter two models thus exhibit more intense anticyclones than cyclones, in line with observations. However, the skewness time series show large fractional changes between simulations with different initial random seeds, as quantified in Table III.

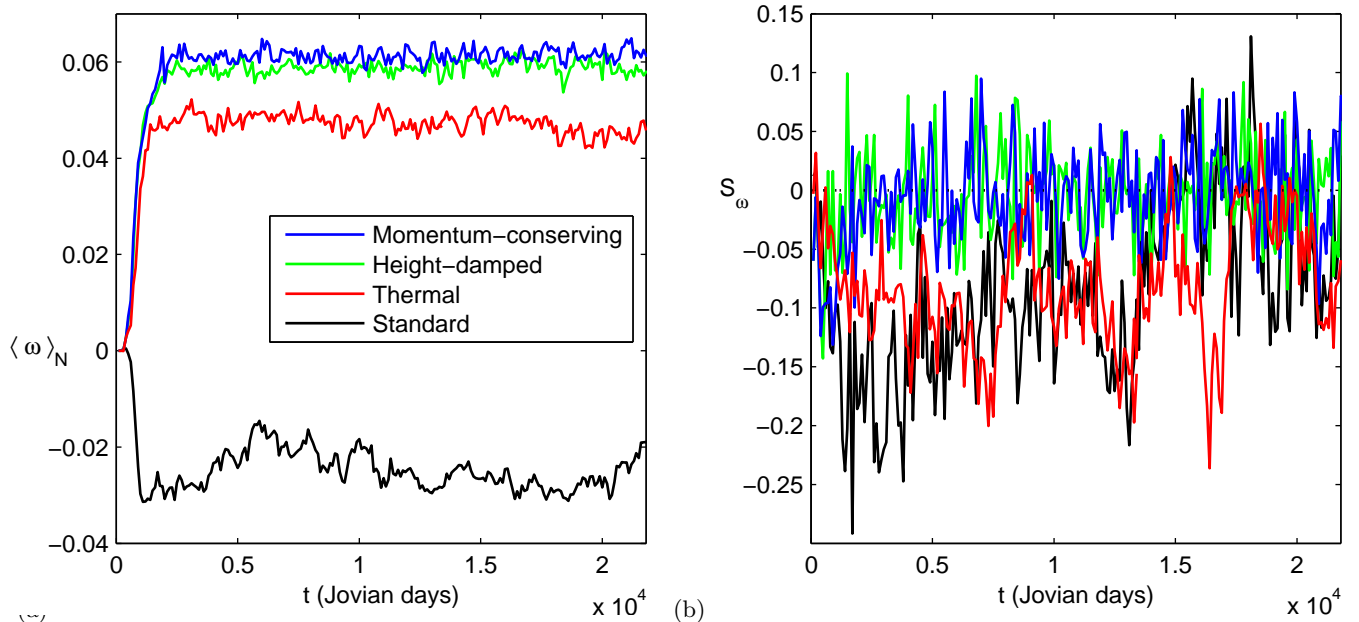


FIG. 9. Evolution of (a) the mean and (b) the skew of the dimensionless relative vorticity. The colors are the same for both plots, and the four curves appear in the same top to bottom order as in the legend for the left-hand plot. In the right-hand plot, S_ω for the two height-damped simulations oscillates around zero, while S_ω for the standard and thermal simulations is distinctly negative.

V. ENERGY SPECTRA FOR JOVIAN SIMULATIONS

We now investigate the energy spectra for simulations of our four different shallow water models in the Jovian parameter regime. Following Scott and Polvani,²⁸ we previously applied narrow-band forcing centred around dimen-

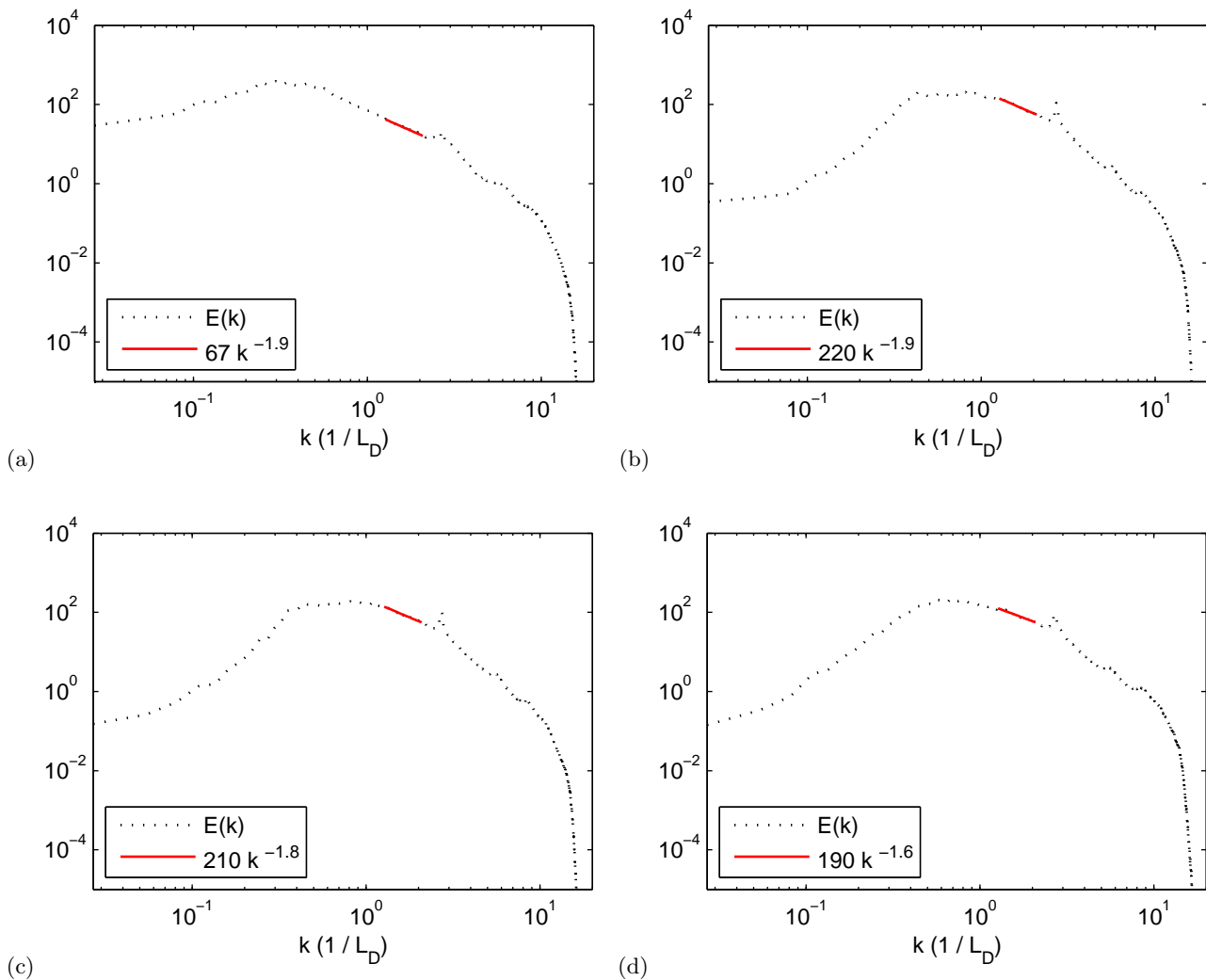


FIG. 10. Non-zonal energy spectra for (a) the standard shallow water model, (b) the height-damped model, (c) the momentum-conserving height-damped model, and (d) the thermal model. Best fit lines to the inertial range are shown solid (red in color).

sionless wavenumber 42. This leads to realistic plots for the field variables, but the resulting inertial range is too small for us to say anything meaningful about the slope of the energy spectrum. We therefore ran further simulations with the forcing centred around dimensionless wavenumber 100, and the other parameters unchanged.

In the absence of rotation, numerical simulations of forced two-dimensional turbulence typically produce energy spectra that follow the classic Kolmogorov scaling $E(k) \propto k^{-5/3}$ in the inertial range, though in two dimensions the inertial range arises from an inverse cascade of energy from the injection scale to larger scales. Analyses of two-dimensional spectra reconstructed from Cassini observations of Jupiter are consistent with an inverse cascade beginning at a dimensionless wavenumber somewhat below 100, as identified by the break in the spectral slope marking the boundary between the inverse and forward cascades.⁶⁹ Coupling to Rossby waves produces a much steeper slope $E(k_x, k_y) \propto k_y^{-5}$ when the zonal wavenumber k_x is small, and the usual scaling $E(k) \propto k^{-5/3}$ elsewhere.⁷⁹ The k_y^{-5} scaling arises from equating the fluid velocity scale $(2E(k_x, k_y)k_y)^{1/2}$ at wavenumber k_y with the Rossby wave phase speed $c_p = -\beta/k_y^2$. This steeper spectrum appears most readily when large-scale friction is weak.⁷⁹

The kinetic energy density $\frac{1}{2}h|\mathbf{u}|^2$ for the shallow water equations is a cubic expression in the field variables h and \mathbf{u} . Replacing h by its mean h_0 gives a quadratic approximation whose spectrum may be computed using standard Fourier techniques based on Parseval’s theorem.^{80,81} This approximation differs from the true kinetic energy by just over 4% for the thermal shallow water simulations at 2×10^4 Jovian days, and by less than 1% for the other three simulations. We believe the higher error in the thermal simulations is due to the presence of an additional force-compensated wave mode in the thermal shallow water equations.⁴⁴ Compensating fluctuations in temperature and height in this mode leave the pressure unchanged, so near geostrophic balance imposes a weaker constraint on the height fluctuations in these equations than in the three non-thermal models. We calculated an average forcing strength $\langle\langle \epsilon_f \rangle\rangle$ over the period from 2×10^4 and 2.18×10^4 Jovian days. We then used the saved simulation output at 2×10^4 days to initialise a new simulation. We ran this simulation with a constant forcing amplitude equal to $\langle\langle \epsilon_f \rangle\rangle$, and calculated an averaged energy spectrum using data from each time step between 2×10^4 and 2.1×10^4 Jovian days.

Figure 10 shows the non-zonal energy spectra $E(k)$ for the four different shallow water models, where “non-zonal” excludes contributions from $k_x = 0$, calculated over the entire simulation domain. All four plots show a peak around the injection wavenumber $L_D k = 200\pi/232 \approx 2.71$. We also show least-squares best fit lines for the inertial ranges,

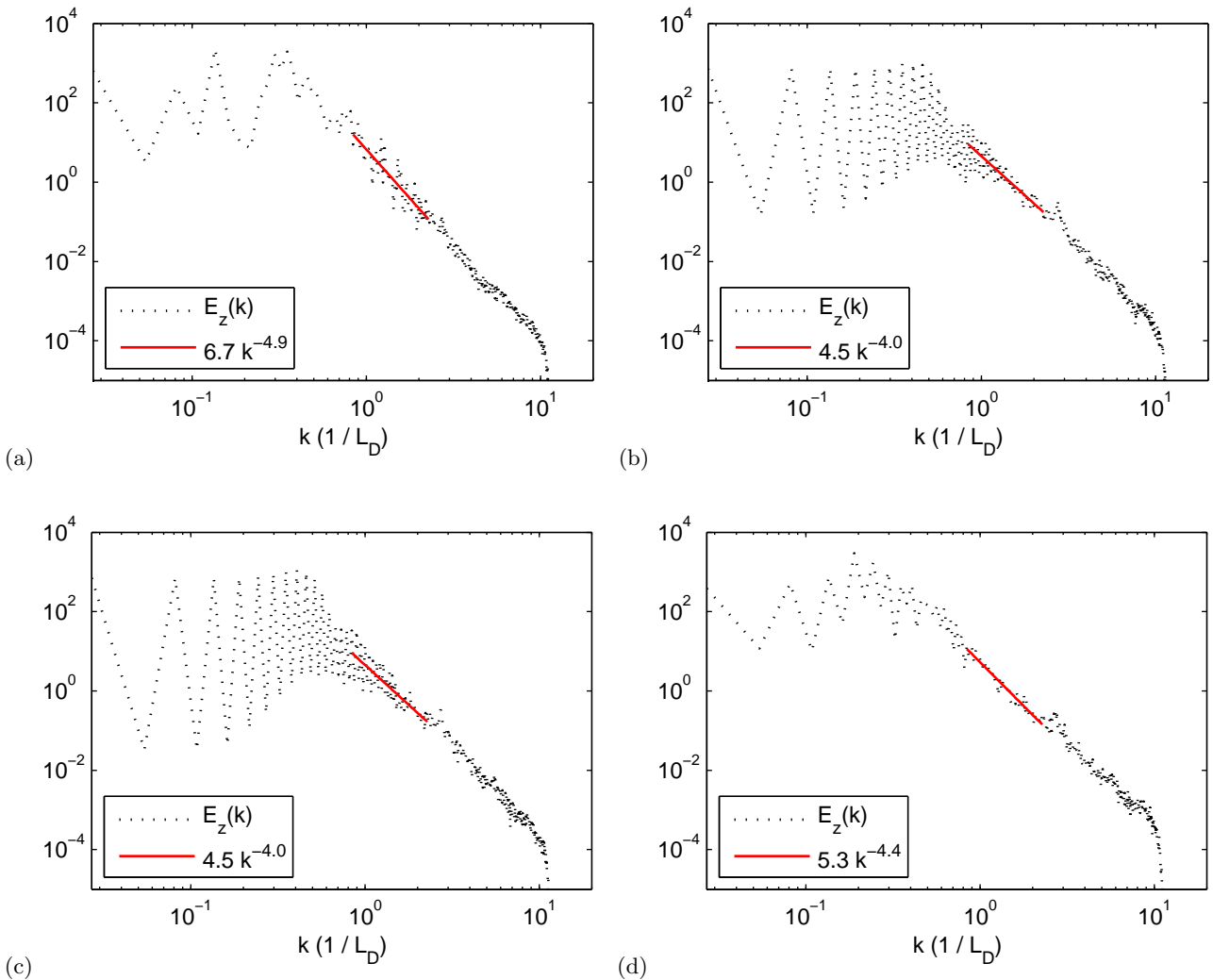


FIG. 11. Zonal energy spectra for (a) the standard shallow water model, (b) the height-damped model, (c) the momentum-conserving height-damped model, and (d) the thermal model. Best fit lines to the inertial range are shown solid (red in color).

each of which has a slope roughly consistent with the Kolmogorov scaling $E(k) \propto k^{-5/3}$.

Figure 11 shows the corresponding zonal energy spectra $E_z(k)$ comprising contributions from $k_x = 0$ (so $k = k_y$) and least-square fits to their inertial ranges. These spectra are much steeper than the Kolmogorov scaling, with slopes ranging between -4.9 and -4.0 . However, they are less steep than the theoretical -5 power law described above.⁷⁹ This is perhaps due to the presence of significant linear drag in our model, which damps the large-scale energy. Galperin *et al.*⁸² fitted slopes of -4.7 ± 1.3 over a short range of wavenumbers to zonal energy spectra obtained from Voyager observations of Jupiter. The slopes of the zonal energy spectra from all four shallow water models lie within these observational error bars.

The zonal energy spectra shown in Fig. 11 exhibit pronounced zig-zag patterns between odd and even wavenumbers, most noticeably for the two height-damped shallow water models. To explain these features, we consider a zonal flow $\bar{u}(y)$ with two top-hat equatorial jets, each of width $2w$, in otherwise quiescent fluid, as sketched in Fig. 12. This crudely approximates the zonal flows shown in Fig. 6. The cosine modes in the Fourier series of $\bar{u}(y)$ all have vanishing coefficients, because $\bar{u}(y)$ is an odd function of y . This explains the zig-zag patterns in Fig. 11, which are due to even modes having significantly smaller coefficients than odd modes.

VI. NEPTUNIAN SIMULATIONS

Cho and Polvani²³ and Scott and Polvani²⁷ performed simulations of the standard rotating shallow water equations in parameter regimes relevant for Uranus and Neptune. They found velocities that were comparable to those of Uranus and Neptune, and a broad, strong retrograde equatorial jet, as observed on Neptune.¹⁵ In this section we present simulations of our thermal shallow water model for Neptunian parameter values, as given in Tables I and II. Neptune is a smaller and colder planet than Jupiter, with only 53 deformation radii around its circumference, compared with 232 for Jupiter. The radiative relaxation time is 396 Neptunian days, compared with 43 Jovian days for Jupiter at the same 25 millibar pressure level. Given the smaller ratio between the domain size and the

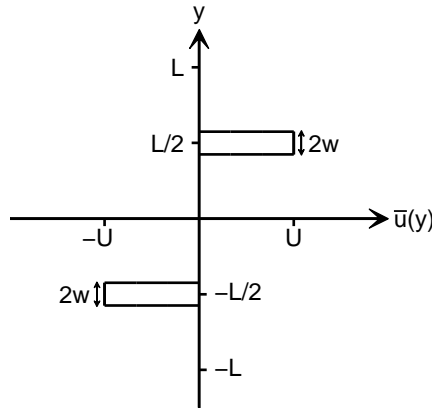


FIG. 12. A step function $\bar{u}(y)$ of period $2L$ which approximates a zonal flow with two equatorial jets in an otherwise quiescent fluid for the square planet domain sketched in Fig. 3.

deformation radius, we centered the forcing at wavenumber $k_c = 10$, rather than the $k_c = 42$ we used for Jupiter. We took $\mathcal{E}_\infty = 2000$, or about 0.71 per unit area, giving a velocity scale $u_{\text{RMS}} \approx 1.19 L_D/T$, so the actual Rossby number is $u_{\text{RMS}}/(2\Omega L_D) \approx 0.095$. A larger \mathcal{E}_∞ would have given larger zonal velocities closer to the observations shown in Fig. 1(b), but the corresponding larger Rossby number implies large free-surface deformations that we found led to unstable simulations. The force-compensated mode allows free-surface deformations in a thermal shallow water simulation to be larger than those in an equivalent standard shallow water simulation with the same Rossby number (see Sec. V). We used the same values for $t_{\text{ramp}} = 1000$ planetary days and $t_{\text{adj}} = 50$ planetary days as before.

These simulations revealed another difficulty that we did not encounter in our Jovian simulations. The zonal momentum equation for the thermal shallow water equations, without forcing or drag, may be written in the conservation form

$$\frac{\partial}{\partial t} \left(h(u + R(y)) \right) + \frac{\partial}{\partial x} \left(hu(u + R(y)) + \frac{1}{2\text{Ro}^2} \Theta h^2 \right) + \frac{\partial}{\partial y} \left(hv(u + R(y)) \right) = 0, \quad (17)$$

where $R(y)$ is the zonal component of the scaled vector potential for the latitude-dependent Coriolis parameter,

$$R(y) = -\frac{1}{\text{Ro}} \int_0^y f(y') dy'. \quad (18)$$

The total zonal momentum over the entire simulation domain thus changes only through forcing and drag, but since this domain contains two planets, the integrated zonal momentum over each individual planet may drift. However, the total momentum over planet 1 had changed by less than 2% after 2×10^4 days in our Jovian simulations. The drifts are larger in our Neptunian simulations, presumably because they contain much larger coherent structures (compare Fig. 13 to Figs. 4 and 5) that transfer significant zonal momentum when they cross the polar lines dividing the two planets. We counteracted these drifts by adding a drag term

$$-\frac{1}{\tau_u h} \left\{ \langle h(u + R(y)) \rangle_{1,2} - \langle R(y) \rangle_{1,2} \right\} \quad (19)$$

to the right hand side of the zonal momentum equation (11c). The notation $\langle \cdot \rangle_{1,2}$ indicates an average over planet 1 when evaluated at points in planet 1, and an average over planet 2 when evaluated at points in planet 2. This term thus causes the total zonal momentum over each of planets 1 and 2 to relax towards its initial value (recall that we take $h = 1$ and $u = 0$ as our initial conditions). We set the relaxation time τ_u to be 200 Neptunian days.

Figure 13 shows the relative vorticity, temperature, and zonal velocity fields after 10^4 Neptunian days for planet 1 in our simulation domain. The correlation between temperature fluctuations and the relative vorticity in the northern hemisphere is -0.09, much smaller in magnitude and the opposite sign to the correlation in our Jovian simulations. The zonal velocity field is far less zonally coherent than the equivalent field for Jupiter shown in Fig. 5(b). Figure 14 shows the instantaneous mean zonal wind \bar{u} in units of Neptunian deformation radii per Neptunian day, with dashed lines showing one standard deviation either side of the mean. The strong retrograde equatorial jet, and two mid-latitude prograde jets, are consistent with observations of Neptune. The large deviations from the zonal mean are consistent with the large error bars and substantial deviations between Hubble Space Telescope and Voyager 2 observations shown in Fig. 1(b), and with the large oscillations in zonal velocities found in more recent Keck Telescope observations.⁸³ However, the maximum zonal wind speed at the equator is significantly weaker than the observed value. We find speeds of around 2 deformation radii per day, while the observations plotted in Fig. 1 are closer to 8 deformation radii per day. The same discrepancy has arisen in previous three-dimensional general circulation model simulations of Neptune,¹⁵ although previous shallow water simulations were able to obtain realistic velocities.^{23,27}

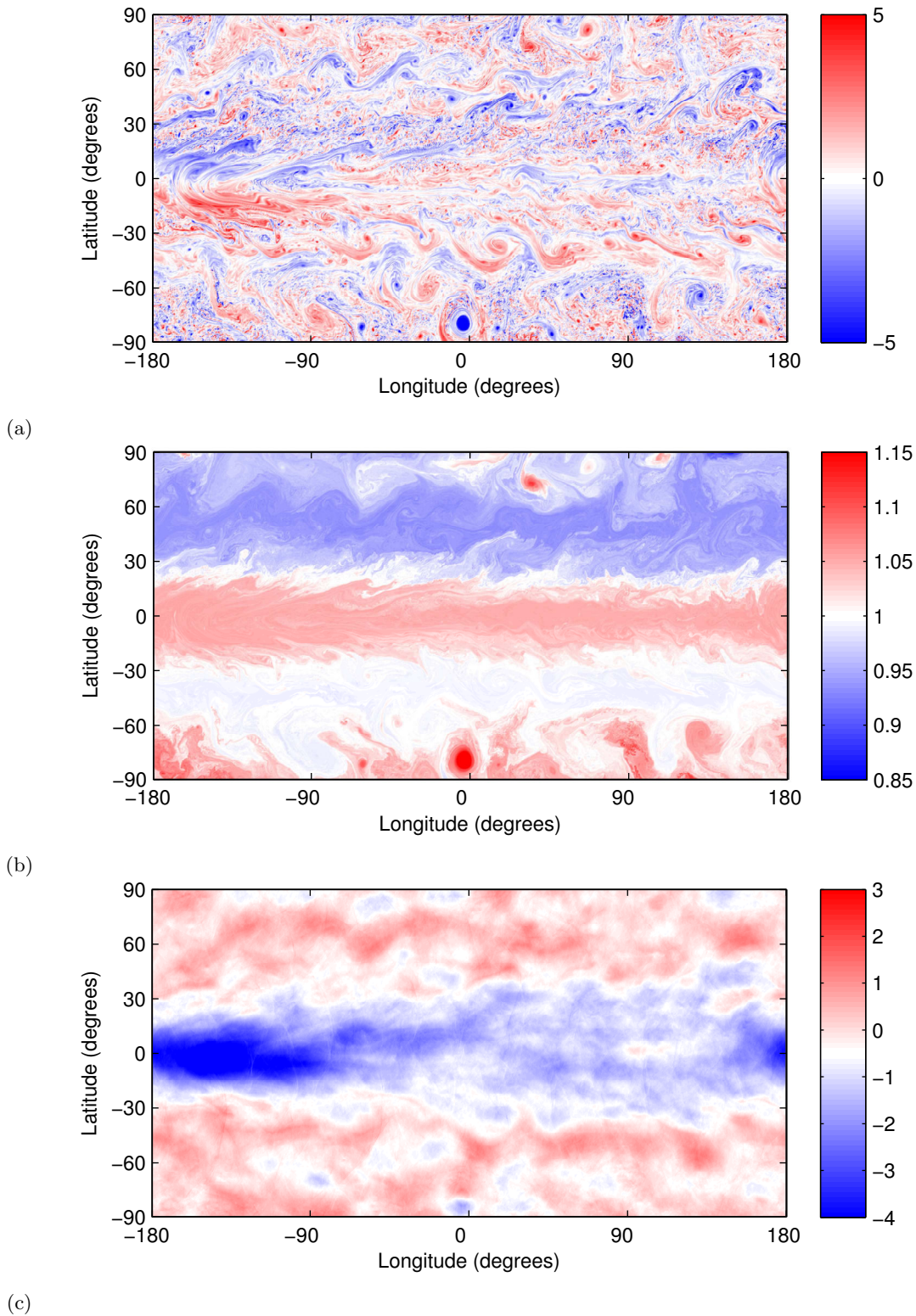


FIG. 13. Dimensionless (a) relative vorticity, (b) temperature, and (c) zonal velocity from a thermal shallow water simulation after 10^4 Neptunian days. Extreme values have been truncated outside the ranges shown on the color bars to show structure at intermediate values more clearly.

VII. CONCLUSIONS

The standard shallow water theory for a single active layer in the equivalent barotropic approximation captures many features of Jovian planetary atmospheres.^{3,18,19,22–25} Forced, dissipative simulations with isotropic random forcing organise themselves into a mixture of alternating zonal jets and long-lived coherent vortices.^{26–28} The approach to a statistically steady state takes many thousands of rotation periods. Some dissipation at large scales, such as Rayleigh friction, appears necessary to dissipate the slow leakage of energy past the Rhines scale that would otherwise cause the jets to break up into large coherent vortices.³ These shallow water simulations all produce retrograde equatorial jets when run for Jovian parameter values, in contrast to the long-lived prograde jets observed on Jupiter and Saturn.

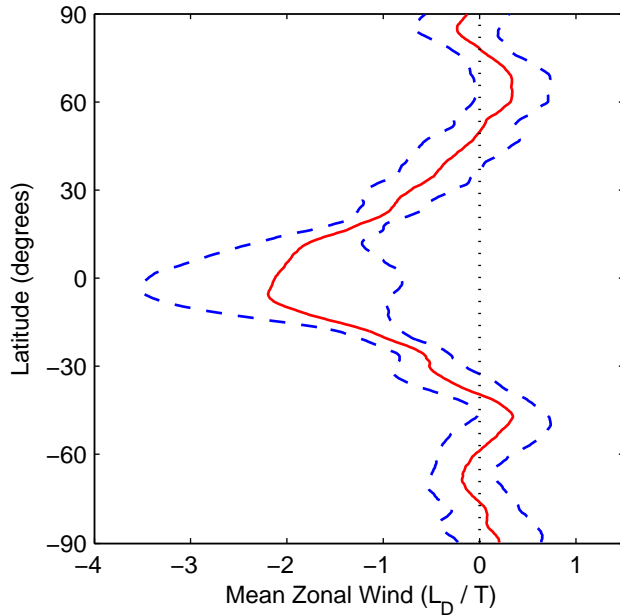


FIG. 14. Mean zonal wind against latitude for Neptune after 10^4 Neptunian days from a thermal shallow water simulation, in units of Neptunian deformation radii per Neptunian day (L_D/T). The dashed lines show one standard deviation either side of the zonal mean.

Scott and Polvani^{27,28} introduced a model for radiative relaxation to equilibrium into the shallow water height equation, following an earlier model for the terrestrial stratosphere.^{33,34} Their simulations produced prograde equatorial jets for Jovian parameters. In this paper we proposed the thermal shallow water equations as an alternative route for introducing radiative relaxation into shallow water theory. These equations extend the standard shallow water theory by treating the reduced gravity as an advected scalar, and so support horizontal variations of thermodynamic properties, such as potential temperature, within the layer.

The addition of radiative cooling to the separate temperature equation leads to a thermal shallow water model for radiative effects in Jovian atmospheres that conserves mass and momentum within the active layer. We performed numerical simulations with four models: our thermal model, the Scott and Polvani model, its momentum-conserving variant, and the standard shallow water model, in a doubly periodic “square planet” geometry that exploits an efficient fast Fourier transform library for graphical processing units (GPUs). We calculated a radiative cooling rate for the 25 millibar pressure level, and imposed a narrow-band isotropic spectral forcing like that employed in many previous simulations.^{27,28,64–66} We controlled the amplitude of the forcing to reach a specified kinetic energy in all four simulations.

Simulations with Jovian parameter values for all four models produced a mixture of vortices and robust zonal jets, whose amplitudes decayed with distance from the equator. The three radiatively damped models each produced a zonal flow that accounted for roughly half the total kinetic energy. They each produced prograde equatorial jets, with the associated net cyclonic vorticity in the northern hemisphere. The standard shallow water model produced a retrograde equatorial jet and net anticyclonic vorticity. The standard and thermal simulations robustly demonstrated more intense anticyclones than cyclones, in accordance with Voyager and Cassini images of Jupiter. Cyclonic regions in the thermal simulation were typically warmer than anticyclonic regions, with a correlation coefficient of 0.29 for the northern hemisphere of planet 1, in qualitative agreement with Jovian observations.³ The standard and thermal shallow water simulations produced substantial jets at mid-latitudes, while the two height-damped shallow water simulations produced a strong equatorial jet with very little activity at other latitudes. This difference was reflected in the kurtosis of the zonal velocity, which was roughly twice as large in the two height-damped models as in the thermal model. Conversely, the thermal model is distinguished by having a larger kurtosis in the relative vorticity than the other three models. All four models produced non-zonal energy spectra slopes that were consistent with the classic Kolmogorov $E(k) \propto k^{-5/3}$ scaling in the inertial range. The zonal energy spectra were all much steeper, though less steep than the $E_z(k) \propto k^{-5}$ predicted by theory. The spectral slopes for all four models lie within the error bars for the slope of the observed zonal energy spectrum for Jupiter.⁸²

We also performed a thermal shallow water simulation for Neptunian parameter values, recalculating the radiative relaxation time at the same 25 millibar pressure level for this much colder planet. Our simulation then produced a retrograde equatorial jet, and two prograde mid-latitude jets, as seen on Neptune, but we were unable to run a stable simulation with sufficient forcing to match the jet speeds seen on Neptune. This may be because the observed maximum jet speed of eight deformation radii per Neptunian day implies a Rossby number close to unity, and hence large deformations of the free surface that destabilise our thermal shallow water model. However, our Neptunian simulation produces velocities closer to those observed on Uranus,¹⁵ and previous papers have used a single simulation to represent both Uranus and Neptune.^{27,84}

Adapting our simulations to run on GPUs gave a substantial (factors of three to five) performance increase over using two conventional multi-core CPUs with little additional programming effort. However our simulations still each took a week to run for 2×10^4 Jovian days at 1024^2 resolution in the Jovian regime, and over two weeks to run in the Neptunian regime. Following the existing global quasi-geostrophic theory for the standard shallow water equations,^{85,86} in future work we will extend our existing local thermal quasi-geostrophic theory⁵³ to develop a global quasi-geostrophic theory for the thermal shallow water equations. This simpler model will help us identify the mechanism responsible for the reversal of the direction of the equatorial jets under sufficiently rapid radiative cooling.

ACKNOWLEDGMENTS

We thank L. N. Chapman and P. L. Read for useful conversations. This work was supported by the UK Engineering and Physical Sciences Research Council through a Doctoral Training Grant award to E.S.W. and an Advanced Research Fellowship [grant number EP/E054625/1] to P.J.D. The computations employed the University of Oxford's Advanced Research Computing facilities, and the Emerald GPU cluster of the e-Infrastructure South Centre for Innovation.

Appendix A: Quasi-geostrophic scaling of the two height-damped shallow water models

The close similarity between our numerical solutions of the two different height-damped shallow water equations is explained by rescaling them for the quasi-geostrophic regime. We consider an f -plane with Coriolis parameter f_0 , and set

$$\mathbf{x} = L\tilde{\mathbf{x}}, \quad \mathbf{u} = U\tilde{\mathbf{u}}, \quad t = (L/U)\tilde{t}, \quad h = h_0 \left(1 + \frac{f_0 U L}{g' h_0} \tilde{\eta} \right), \quad (\text{A1})$$

where L and U are horizontal length and velocity scales respectively, h_0 is the mean layer depth, and g' is the reduced gravity. A superscript tilde denotes a dimensionless variable or operator. The momentum-conserving height-damped shallow water equations, corresponding to (4) with the Heaviside function omitted as in (10), become

$$\text{Ro} \left(\tilde{\eta}_{\tilde{t}} + \tilde{\nabla} \cdot (\tilde{\eta} \tilde{\mathbf{u}}) \right) + \text{Bu} \tilde{\nabla} \cdot \tilde{\mathbf{u}} = -\kappa \text{Ro} \tilde{\eta}, \quad (\text{A2a})$$

$$\text{Ro} \left(\tilde{\mathbf{u}}_{\tilde{t}} + \tilde{\mathbf{u}} \cdot \tilde{\nabla} \tilde{\mathbf{u}} \right) + \hat{\mathbf{z}} \times \tilde{\mathbf{u}} = -\tilde{\nabla} \tilde{\eta} + \text{Ro}^2 \frac{\kappa}{\text{Bu} + \text{Ro} \tilde{\eta}} \tilde{\eta} \tilde{\mathbf{u}}, \quad (\text{A2b})$$

with parameters

$$\text{Ro} = U/(f_0 L), \quad \text{Bu} = g' h_0 / (f_0^2 L^2), \quad \text{and} \quad \kappa = 1/(\text{Ro} f_0 \tau_{\text{rad}}). \quad (\text{A3})$$

We have scaled the radiative damping term on the right hand side of (A2a) to balance the time derivative on the left hand side, as in our earlier quasi-geostrophic scaling of the thermal shallow water equations.⁵³ This scaling preserves $\tilde{\nabla} \cdot \tilde{\mathbf{u}} = O(\text{Ro})$, which lets us introduce a geostrophic streamfunction to write $\tilde{\mathbf{u}} = \hat{\mathbf{z}} \times \tilde{\nabla} \tilde{\psi}$. Having chosen this scaling, the only difference between this momentum-conserving model and the rescaled version of the non-momentum-conserving Scott and Polvani model^{27,28} is the $O(\text{Ro}^2)$ last term that appears in (A2b). The two models thus become identical in the quasi-geostrophic approximation that retains only $O(\text{Ro})$ corrections to geostrophic balance. The quasi-geostrophic potential vorticity equation is

$$\tilde{q}_{\tilde{t}} + \hat{\mathbf{z}} \cdot \left(\tilde{\nabla} \tilde{\psi} \times \tilde{\nabla} \tilde{q} \right) = (\kappa/\text{Bu}) \tilde{\psi}, \quad \text{where} \quad \tilde{q} = \tilde{\nabla}^2 \tilde{\psi} - \tilde{\psi}/\text{Bu}. \quad (\text{A4})$$

The radiative height damping thus appears as a hypoviscous dissipation with coefficient $\kappa/\text{Bu} = f_0^2 L^3 / (g' h_0 U \tau_{\text{rad}})$ proportional to the square of the Coriolis parameter f_0 .²⁷

¹N. A. Maximenko, B. Bang, and H. Sasaki, *Observational evidence of alternating zonal jets in the world ocean*, Geophys. Res. Lett. **32**, L12607 (2005).

²K. J. Richards, N. A. Maximenko, F. O. Bryan, and H. Sasaki, *Zonal jets in the Pacific Ocean*, Geophys. Res. Lett. **33**, L03605 (2006).

³A. R. Vasavada and A. P. Showman, *Jovian atmospheric dynamics: an update after Galileo and Cassini*, Rep. Prog. Phys. **68**, 1935 (2005).

⁴S. S. Limaye, *Jupiter: New estimates of the mean zonal flow at the cloud level*, Icarus **65**, 335 (1986).

⁵C. C. Porco, R. A. West, A. McEwen, A. D. Del Genio, A. P. Ingersoll, P. Thomas, S. Squyres, L. Dones, C. D. Murray, T. V. Johnson, et al., *Cassini imaging of Jupiter's atmosphere, satellites, and rings*, Science **299**, 1541 (2003).

⁶L. A. Sromovsky, P. M. Fry, T. E. Dowling, K. H. Baines, and S. S. Limaye, *Coordinated 1996 HST and IRTF imaging of Neptune and Triton: III. Neptune's atmospheric circulation and cloud structure*, Icarus **149**, 459 (2001).

⁷D. H. Atkinson, J. B. Pollack, and A. Seiff, *The Galileo Probe Doppler wind experiment: Measurement of the deep zonal winds on Jupiter*, J. Geophys. Res. **103**, 22911 (1998).

⁸P. J. Gierasch, *Jovian meteorology: Large-scale moist convection*, Icarus **29**, 445 (1976).

⁹A. P. Ingersoll, *Atmospheric dynamics of the outer planets*, Science **248**, 308 (1990).

¹⁰J. A. Magalhães, A. Seiff, and R. E. Young, *The stratification of Jupiter's troposphere at the Galileo Probe entry site*, Icarus **158**, 410 (2002).

- ¹¹A. P. Ingersoll, T. E. Dowling, P. J. Gierasch, G. S. Orton, P. L. Read, A. Sánchez-Lavega, A. P. Showman, A. A. Simon-Miller, and A. R. Vasavada, *Dynamics of Jupiter's atmosphere*, in *Jupiter: The Planet, Satellites and Magnetosphere*, edited by F. Bagenal, T. E. Dowling, and W. B. McKinnon (Cambridge University Press, Cambridge, 2007), pp. 105–128.
- ¹²T. E. Dowling, *Estimate of Jupiter's deep zonal-wind profile from Shoemaker–Levy 9 data and Arnold's second stability criterion*, *Icarus* **117**, 439 (1995).
- ¹³R. Beebe, *Characteristic zonal winds and long-lived vortices in the atmospheres of the outer planets*, *Chaos* **4**, 113 (1994).
- ¹⁴M. Heimpel and J. Aurnou, *Turbulent convection in rapidly rotating spherical shells: A model for equatorial and high latitude jets on Jupiter and Saturn*, *Icarus* **187**, 540 (2007).
- ¹⁵J. Liu and T. Schneider, *Mechanisms of jet formation on the giant planets*, *J. Atmos. Sci.* **67**, 3652 (2010).
- ¹⁶L. A. Sromovsky, S. S. Limaye, and P. M. Fry, *Dynamics of Neptune's major cloud features*, *Icarus* **105**, 110 (1993).
- ¹⁷G. P. Williams, *Planetary circulations: 1. Barotropic representation of Jovian and terrestrial turbulence*, *J. Atmos. Sci.* **35**, 1399 (1978).
- ¹⁸T. E. Dowling and A. P. Ingersoll, *Jupiter's Great Red Spot as a shallow water system*, *J. Atmos. Sci.* **46**, 3256 (1989).
- ¹⁹P. S. Marcus, *Numerical simulation of Jupiter's Great Red Spot*, *Nature* **331**, 693 (1988).
- ²⁰G. P. Williams and T. Yamagata, *Geostrophic regimes, intermediate solitary vortices and Jovian eddies*, *J. Atmos. Sci.* **41**, 453 (1984).
- ²¹G. P. Williams and R. J. Wilson, *The stability and genesis of Rossby vortices*, *J. Atmos. Sci.* **45**, 207 (1988).
- ²²J. Y.-K. Cho and L. M. Polvani, *The emergence of jets and vortices in freely evolving, shallow-water turbulence on a sphere*, *Phys. Fluids* **8**, 1531 (1996).
- ²³J. Y.-K. Cho and L. M. Polvani, *The morphogenesis of bands and zonal winds in the atmospheres on the giant outer planets*, *Science* **273**, 335 (1996).
- ²⁴R. Iacono, M. V. Struglia, C. Ronchi, and S. Nicastro, *High-resolution simulations of freely decaying shallow-water turbulence on a rotating sphere*, *Il Nuovo Cimento C* **22**, 813 (1999).
- ²⁵R. Iacono, M. V. Struglia, and C. Ronchi, *Spontaneous formation of equatorial jets in freely decaying shallow water turbulence*, *Phys. Fluids* **11**, 1272 (1999).
- ²⁶A. P. Showman, *Numerical simulations of forced shallow-water turbulence: Effects of moist convection on the large-scale circulation of Jupiter and Saturn*, *J. Atmos. Sci.* **64**, 3132 (2007).
- ²⁷R. K. Scott and L. M. Polvani, *Forced-dissipative shallow-water turbulence on the sphere and the atmospheric circulation of the giant planets*, *J. Atmos. Sci.* **64**, 3158 (2007).
- ²⁸R. K. Scott and L. M. Polvani, *Equatorial superrotation in shallow atmospheres*, *Geophys. Res. Lett.* **35**, L24202 (2008).
- ²⁹A. E. Gill, *Atmosphere Ocean Dynamics* (Academic Press, New York, 1982).
- ³⁰G. K. Vallis, *Atmospheric and Oceanic Fluid Dynamics* (Cambridge University Press, Cambridge, 2006).
- ³¹P. B. Rhines, *Waves and turbulence on a beta-plane*, *J. Fluid Mech.* **69**, 417 (1975).
- ³²Y. Kitamura and K. Ishioka, *Equatorial jets in decaying shallow-water turbulence on a rotating sphere*, *J. Atmos. Sci.* **64**, 3340 (2007).
- ³³M. Jukes, *A shallow water model of the winter stratosphere*, *J. Atmos. Sci.* **46**, 2934 (1989).
- ³⁴L. M. Polvani, D. W. Waugh, and R. A. Plumb, *On the subtropical edge of the stratospheric surf zone*, *J. Atmos. Sci.* **52**, 1288 (1995).
- ³⁵K. M. Shell and I. M. Held, *Abrupt transition to strong superrotation in an axisymmetric model of the upper troposphere*, *J. Atmos. Sci.* **61**, 2928 (2004).
- ³⁶R. L. Lavoie, *A mesoscale numerical model of lake-effect storms*, *J. Atmos. Sci.* **29**, 1025 (1972).
- ³⁷P. S. Schopf and M. A. Cane, *On equatorial dynamics, mixed layer physics and sea surface temperature*, *J. Phys. Oceanogr.* **13**, 917 (1983).
- ³⁸J. P. McCreary and Z. Yu, *Equatorial dynamics in a $2\frac{1}{2}$ -layer model*, *Prog. Oceanogr.* **29**, 61 (1992).
- ³⁹J. P. McCreary and P. K. Kundu, *A numerical investigation of the Somali Current during the Southwest Monsoon*, *J. Marine Res.* **46**, 25 (1988).
- ⁴⁰J. P. McCreary, Y. Fukumachi, and P. K. Kundu, *A numerical investigation of jets and eddies near an eastern ocean boundary*, *J. Geophys. Res.* **96**, 2515 (1991).
- ⁴¹L. P. Røed and X. B. Shi, *A numerical study of the dynamics and energetics of cool filaments, jets, and eddies off the Iberian Peninsula*, *J. Geophys. Res.* **104**, 29,817 (1999).
- ⁴²P. Ripa, *Conservation laws for primitive equations models with inhomogeneous layers*, *Geophys. Astrophys. Fluid Dynam.* **70**, 85 (1993).
- ⁴³P. Ripa, *On improving a one-layer ocean model with thermodynamics*, *J. Fluid Mech.* **303**, 169 (1995).
- ⁴⁴P. Ripa, *Linear waves in a one-layer ocean model with thermodynamics*, *J. Geophys. Res.* **101**, 1233 (1996).
- ⁴⁵F. Bouchut, J. Lambaerts, G. Lapeyre, and V. Zeitlin, *Fronts and nonlinear waves in a simplified shallow-water model of the atmosphere with moisture and convection*, *Phys. Fluids* **21**, 116604 (2009).
- ⁴⁶J. Lambaerts, G. Lapeyre, V. Zeitlin, and F. Bouchut, *Simplified two-layer models of precipitating atmosphere and their properties*, *Phys. Fluids* **23**, 046603 (2011).
- ⁴⁷P. A. Gilman, *Magnetohydrodynamic "shallow water" equations for the solar tachocline*, *Astrophys. J. Lett.* **544**, L79 (2000).
- ⁴⁸P. J. Dellar, *Common Hamiltonian structure of the shallow water equations with horizontal temperature gradients and magnetic fields*, *Phys. Fluids* **15**, 292 (2003).
- ⁴⁹D. J. Stevenson and E. E. Salpeter, *Interior models of Jupiter*, in *Jupiter: Studies of the Interior, Atmosphere, Magnetosphere and Satellites*, edited by T. Gehrels (University of Arizona Press, Tucson, 1976), pp. 85–112.
- ⁵⁰T. Guillot, D. J. Stevenson, W. B. Hubbard, and D. Saumon, *The interior of Jupiter*, in *Jupiter: The Planet, Satellites and Magnetosphere*, edited by F. Bagenal, T. E. Dowling, and W. B. McKinnon (Cambridge University Press, Cambridge, 2007), pp. 35–57.
- ⁵¹A. P. Ingersoll and J. N. Cuzzi, *Dynamics of Jupiter's cloud bands*, *J. Atmos. Sci.* **26**, 981 (1969).
- ⁵²A. P. Ingersoll, R. F. Beebe, B. J. Conrath, and G. E. Hunt, *Structure and dynamics of Saturn's atmosphere*, in *Saturn*, edited by T. Gehrels and M. S. Matthews (University of Arizona Press, Tucson, 1984), pp. 195–238.
- ⁵³E. S. Warnford and P. J. Dellar, *The quasi-geostrophic theory of the thermal shallow water equations*, *J. Fluid Mech.* **723**, 374 (2013).
- ⁵⁴J. Miles and R. Salmon, *Weakly dispersive nonlinear gravity waves*, *J. Fluid Mech.* **157**, 519 (1985).
- ⁵⁵W. R. Young, *The subinertial mixed layer approximation*, *J. Phys. Oceanogr.* **24**, 1812 (1994).
- ⁵⁶A. P. Ingersoll, P. J. Gierasch, D. Banfield, A. R. Vasavada, and the Galileo Imaging Team, *Moist convection as an energy source for the large-scale motions in Jupiter's atmosphere*, *Nature* **403**, 630 (2000).
- ⁵⁷J. Houghton, *The Physics of Atmospheres* (Cambridge University Press, 2002).
- ⁵⁸A. Seiff, D. B. Kirk, T. C. D. Knight, R. E. Young, J. D. Mihalov, L. A. Young, F. S. Milos, G. Schubert, R. C. Blanchard, and D. Atkinson, *Thermal structure of Jupiter's atmosphere near the edge of a 5- μ m hot spot in the north equatorial belt*, *J. Geophys. Res.* **103**, 22,857 (1998).
- ⁵⁹S. Yoden and M. Yamada, *A numerical experiment on two-dimensional decaying turbulence on a rotating sphere*, *J. Atmos. Sci.* **50**, 631 (1993).
- ⁶⁰S. Yoden, K. Ishioka, Y.-Y. Hayashi, and M. Yamada, *A further experiment on two-dimensional decaying turbulence on a rotating sphere*, *Il Nuovo Cimento C* **22**, 803 (1999).
- ⁶¹I. O. Hupca, J. Falcou, L. Grigori, and R. Stompor, *Spherical harmonic transform with GPUs*, *Lecture Notes in Computer Science* **7155**, 355 (2012).

- ⁶²T. Y. Hou and R. Li, *Computing nearly singular solutions using pseudo-spectral methods*, J. Comput. Phys. **226**, 379 (2007).
- ⁶³D. K. Lilly, *Numerical simulation of two-dimensional turbulence*, Phys. Fluids **12**, II-240 (1969).
- ⁶⁴K. S. Smith, G. Boccaletti, C. C. Henning, I. Marinov, C. Y. Tam, I. M. Held, and G. K. Vallis, *Turbulent diffusion in the geostrophic inverse cascade*, J. Fluid Mech. **469**, 13 (2002).
- ⁶⁵K. S. Smith, *A local model for planetary atmospheres forced by small-scale convection*, J. Atmos. Sci. **61**, 1420 (2004).
- ⁶⁶K. Srinivasan and W. R. Young, *Zonostrophic instability*, J. Atmos. Sci. **69**, 1633 (2012).
- ⁶⁷R. Salmon, *Baroclinic instability and geostrophic turbulence*, Geophysical & Astrophysical Fluid Dynamics **15**, 167 (1980).
- ⁶⁸R. K. Scott, *Nonrobustness of the two-dimensional turbulent inverse cascade*, Phys. Rev. E **75**, 046301 (2007).
- ⁶⁹D. S. Choi and A. P. Showman, *Power spectral analysis of Jupiter's clouds and kinetic energy from Cassini*, Icarus **216**, 597 (2011).
- ⁷⁰P. H. Hünenberger, *Thermostat algorithms for molecular dynamics simulations*, Adv. Polym. Sci. **173**, 105 (2005).
- ⁷¹M. Matsumoto and T. Nishimura, *Mersenne twister: a 623-dimensionally equidistributed uniform pseudo-random number generator*, ACM Trans. Model. Comput. Simul. **8**, 3 (1998).
- ⁷²R. S. Wikramaratna, *ACORN – A new method for generating sequences of uniformly distributed pseudo-random numbers*, J. Comput. Phys. **83**, 16 (1989).
- ⁷³T. Schneider and J. Liu, *Formation of Jets and Equatorial Superrotation on Jupiter*, J. Atmos. Sci. **66**, 579 (2009).
- ⁷⁴J. C. McWilliams, *The emergence of isolated coherent vortices in turbulent flow.*, J. Fluid Mech. **146**, 21 (1984).
- ⁷⁵J. B. Weiss and J. C. McWilliams, *Temporal scaling behavior of decaying two-dimensional turbulence*, Phys. Fluids A **5**, 608 (1993).
- ⁷⁶L. M. Polvani, J. C. McWilliams, M. A. Spall, and R. Ford, *The coherent structures of shallow-water turbulence: Deformation-radius effects, cyclone/anticyclone asymmetry and gravity-wave generation*, Chaos **4**, 177 (1994).
- ⁷⁷M.-M. Mac Low and A. P. Ingersoll, *Merging of vortices in the atmosphere of Jupiter: An analysis of Voyager images*, Icarus **65**, 353 (1986).
- ⁷⁸L. Li, A. P. Ingersoll, A. R. Vasavada, C. C. Porco, A. D. Del Genio, and S. P. Ewald, *Life cycles of spots on Jupiter from Cassini images*, Icarus **172**, 9 (2004).
- ⁷⁹H.-P. Huang, B. Galperin, and S. Sukoriansky, *Anisotropic spectra in two-dimensional turbulence on the surface of a rotating sphere*, Phys. Fluids **13**, 225 (2001).
- ⁸⁰T. Warn, *Statistical mechanical equilibria of the shallow water equations*, Tellus A **38**, 1 (1986).
- ⁸¹M. Farge and R. Sadourny, *Wave-vortex dynamics in rotating shallow water*, J. Fluid Mech. **206**, 433 (1989).
- ⁸²B. Galperin, S. Sukoriansky, and H.-P. Huang, *Universal n^{-5} spectrum of zonal flows on giant planets*, Phy. Fluids **13**, 1545 (2001).
- ⁸³S. C. Martin, I. Pater, and P. Marcus, *Neptune's zonal winds from near-IR Keck adaptive optics imaging in August 2001*, Astrophys. Space Sci. **337**, 65 (2012).
- ⁸⁴Y. Lian and A. P. Showman, *Generation of equatorial jets by large-scale latent heating on the giant planets*, Icarus **207**, 373 (2010).
- ⁸⁵W. H. Schubert, R. K. Taft, and L. G. Silvers, *Shallow water quasi-geostrophic theory on the sphere*, J. Adv. Model. Earth Syst. **1**, 2 (2009).
- ⁸⁶W. T. M. Verkley, *A balanced approximation of the one-layer shallow-water equations on a sphere*, J. Atmos. Sci. **66**, 1735 (2009).